Available online at www.sciencedirect.com
ScienceDirect
Comput. Methods Appl. Mech. Engrg. 400 (2022) 115489
Computer methods in applied mechanics and engineering
www.elsevier.com/locate/cma

Semi-implicit fluid–structure interaction in biomedical applications

Richard Schussnig[a,b,*], Douglas R.Q. Pacheco[c], Manfred Kaltenbacher[b,d], Thomas-Peter Fries[a,b]

[a] *Institute of Structural Analysis, Graz University of Technology, Lessingstraße 25/II, Graz, 8010, Styria, Austria*
[b] *Graz Center of Computational Engineering, Graz University of Technology, Krenngasse 37/I, Graz, 8010, Styria, Austria*
[c] *Department of Mathematical Sciences, Norwegian University of Science and Technology, Alfred Getz' vei 1, Trondheim, 7034, Trøndelag, Norway*
[d] *Institute of Fundamentals and Theory in Electrical Engineering, Graz University of Technology, Inffeldgasse 18/I, Graz, 8010, Styria, Austria*

Received 4 May 2022; received in revised form 27 July 2022; accepted 27 July 2022
Available online 12 August 2022

Abstract

Fluid–structure interaction (FSI) incorporates effects of fluid flows on deformable solids and vice versa. Complex biomedical problems in clinical applications continue to challenge numerical algorithms, as incorporating the underlying mathematical methods can impair the solvers' performance drastically. In this regard, we extend a semi-implicit, pressure Poisson-based FSI scheme for non-Newtonian fluids to incorporate several models crucial for biomechanical applications. We consider Windkessel outlets to account for neglected downstream flow regions, realistic material fibre orientation and stressed reference geometries reconstructed from medical image data. Additionally, we incorporate vital numerical aspects, namely, stabilisations to counteract dominant convective effects and instabilities triggered by re-entrant flow, while a major contribution of this work is combining interface quasi-Newton methods with Robin coupling conditions to accelerate the partitioned (semi-)implicit coupling scheme. The numerical examples presented herein aim to finally bridge the gap to real-world applications, considering state-of-the-art modelling aspects and physiological parameters. FSI simulations of blood flow in an iliac bifurcation derived from medical images and vocal folds deforming in the process of human phonation demonstrate the versatility of the framework.

MSC: 74F10; 76A05; 76M10; 74L15; 76D05

Keywords: Semi-implicit coupling; Fractional-step time-marching; Fluid–structure interaction; Non-Newtonian fluid; Patient-specific simulation; Navier–Stokes equations

1. Introduction

Rapid progress in computational (bio-)mechanics continues to increase the reliability and significance of patient-specific simulations. In clinical decision making, treatment planning, prototyping and testing on virtual cohorts, both costs and ethical concerns can be mitigated when compared to traditional in-vivo studies. As numerical methods continue to advance, computational tools are employed for increasingly complex tasks, where individual mathematical models may have an even stronger impact on the overall algorithm. In biomedical engineering, many

* Corresponding author at: Institute of Structural Analysis, Graz University of Technology, Lessingstraße 25/II, Graz, 8010, Styria, Austria.
E-mail address: schussnig@tugraz.at (R. Schussnig).

https://doi.org/10.1016/j.cma.2022.115489

of these applications feature incompressible flow interacting with soft biological tissue, leading to a fluid–structure interaction (FSI) problem. Whether the task involves blood flow [1–3], human phonation [4–7] or respiration [8,9], the fundamental theme of a deforming flow domain plays a central role in the system's behaviour.

To account for fluid domain motion, arbitrary Lagrangian–Eulerian (ALE) techniques [10–12], immersed boundary methods [13,14] and fictitious-domain approaches [15,16] are the most popular techniques. Ensuring continuity of velocities, displacements and tractions requires enforcing coupling conditions on the moving fluid–solid interface via, e.g., Lagrange multipliers [17,18], Nitsche's method [19,20], mortar techniques [14,21], penalty approaches [22,23], formulations allowing for globally continuous function spaces [24–27] or other concepts. The interface data is updated in each step of an iterative, partitioned scheme [28,29], exchanging data of the individual field's solvers in each pass, or by solving a single monolithic system [10,17,18,27,30].

In biomedical applications, robust convergence of the coupling algorithm and numerical stability with respect to physical parameters are particularly important. Depending on the solid and fluid density ratio, the slenderness of the computational domain and the time step size, the so-called added-mass effect [31,32] can significantly reduce the efficiency of traditional partitioned setups. Nonetheless, the partitioned design offers increased modularity and exchangeability, motivating efforts towards easing the numerical treatment. In this regard, it has been shown that dynamic relaxation [9], interface (quasi-)Newton schemes [33,34], interface Newton–Krylov methods [35,36], artificial compressibility [37,38] or Robin interface conditions can yield considerable improvements.

Simultaneously, semi-implicit treatment of the momentum and mass balance equations and coupling conditions, as initially proposed by Fernández [39], led to significant advances in the field. Based on projection or time-splitting methods for the fluid phase, proper linearisation and extrapolation allows treating the fluid momentum balance equations, mesh motion equation and possibly other equations outside of the iterative coupling loop (see, e.g., [11,40–42]). Recent developments enable fully explicit treatment of interface conditions for selected FSI problems even with large added-mass effect, both for shells [43–46] and three-dimensional continua [47–50]. Depending on the software design, generality, problem parameters and involved models, those fully explicit coupling schemes for bulk continua are very promising, but are still either limited to the simplest constitutive laws and first-order temporal accuracy, or involve a multitude of correction steps.

Applying such schemes to practically relevant problems in bioengineering or clinical application is another important hurdle to be taken. Including additional modelling aspects to account for realistic conditions or targeting physiologically relevant parameters can have a drastic impact on runtimes and stability. For both coupled velocity–pressure and projection schemes, well-established methods exist to account for the downstream vasculature via lumped parameter models and to counteract instabilities arising in the case of backflow. Similarly, numerical techniques to accelerate the convergence of the FSI coupling algorithm are readily available and thoroughly tested for coupled velocity–pressure formulations used in the fluid solver, but rarely presented for split-step schemes [41,51].

This work extends our basic formulation [52], which is a partitioned FSI solver based on a consistent split-step scheme. Therein, a pressure Poisson equation (PPE) allowing for variable viscosity and including fully consistent boundary conditions is used to recover the pressure. This enables added-mass-stable coupling by iteratively solving only the PPE and structure subproblems. However, the original contribution [52] did not demonstrate improved convergence using Robin interface conditions, used only trivial acceleration schemes and did not include any further models arising in clinical applications.

Herein, we carefully integrate well-established mathematical models and numerical techniques into the PPE-based FSI scheme [52], preserving accuracy, efficiency and stability. The approaches to reduce instabilities arising in the practical parameter range are (i) backflow stabilisation [53], and (ii) Galerkin least-squares stabilisation (GLS) [54] for dominant convection, each of which shall here be introduced in all necessary detail. To counteract decreasing convergence speed as the added-mass effect becomes dominant, we consider (iii) Robin interface conditions and (iv) the interface quasi-Newton inverse least-squares method (IQN-ILS) [33]. Compared to [52], we will show how this combination can lead to a robust and accurate numerical tool suitable for application in practical problems – a key contribution of this work. Regarding mathematical models in the cardiovascular and general biomedical context, we consider (i) three-element Windkessel models to account for the downstream vasculature's resistance and capacitance, (ii) remapping of prescribed inflow profiles to non-circular inlets [55], (iii) construction of material orientation vectors in tube-like geometries with subdivided cross sections and (iv) an algorithm to include prestress present in geometries constructed from medical images [56]. Building up from [52], we investigate how the velocity interpolation affects the temporal stability, which can pose a challenge to the coupling scheme, especially when

considering Windkessel models and adaptive timestepping. Additionally, a new orientation algorithm modified from [3] to tackle dissected vessel trees is presented, eliminating the need for detecting vessel regions.

The remainder of this article is organised as follows: Section 2 introduces the basic version of the PPE-based FSI solver [52] and its semi-implicit variants, the semi-implicit Dirichlet–Neumann (SIDN) and semi-implicit Dirichlet–Robin (SIDR) schemes. Numerical methods, i.e., backflow stabilisation, GLS and IQN-ILS acceleration to increase robustness and stability and to lower the amount of FSI coupling iterations are introduced in Section 3. Thereafter, Section 4 describes proper inclusion of lumped-parameter models in the split-step scheme, the construction of material orientations for complex geometries and a suitable prestress algorithm. In Section 5, several numerical experiments from vastly different biomechanical FSI applications – blood flow through straight and bifurcating vessels and airflow through the vocal folds – showcase the versatility and robustness of the framework. Conclusions and limitations are discussed in the closing Section 6.

2. Problem statement

The FSI problem defined on the moving domain Ω^t couples incompressible flows of generalised Newtonian fluids in the fluid domain $\Omega_f^t \subset \Omega^t$ with elastic continua occupying $\Omega_s^t = \Omega^t \setminus \Omega_f^t$. The subdomains share the interface denoted as $\Sigma^t := \partial\Omega_s^t \cap \partial\Omega_f^t$, where displacements, velocities and tractions are continuous,

$$\boldsymbol{d}_s = \boldsymbol{d}_f, \quad \frac{\partial}{\partial t}\boldsymbol{d}_s = \boldsymbol{u}_f, \quad \boldsymbol{\sigma}_f \boldsymbol{n}_f = \boldsymbol{\sigma}_s \boldsymbol{n}_f, \tag{1}$$

with $\boldsymbol{d}_s$ and $\boldsymbol{d}_f$ being the solid and fluid displacements from the reference configuration, the fluid velocity $\boldsymbol{u}_f$ in the spatial configuration, the Cauchy stresses $\boldsymbol{\sigma}_s$ and $\boldsymbol{\sigma}_f$, $\frac{\partial}{\partial t}\boldsymbol{d}_s$ denoting the solid's material velocity and $\boldsymbol{n}_f$ the unit outward normal on Ω_f^t. The fluid domain displacement $\boldsymbol{d}_f$ allows to conveniently describe the domain motion over time in an ALE framework. On a joint static reference frame $\hat{\Omega} := \hat{\Omega}_f \cup \hat{\Omega}_s$, the maps

$$\mathcal{A}_t : \hat{\Omega}_f \to \Omega_f^t, \quad \mathcal{A}_t = \hat{\boldsymbol{x}} + \boldsymbol{d}_f(\hat{\boldsymbol{x}}, t), \qquad \mathcal{L}_t : \hat{\Omega}_s \to \Omega_s^t, \quad \mathcal{L}_t = \hat{\boldsymbol{x}} + \boldsymbol{d}_s(\hat{\boldsymbol{x}}, t),$$

with respective deformation gradients $\boldsymbol{F}$ and Jacobians J

$$\boldsymbol{F}_f := \boldsymbol{I} + \nabla \boldsymbol{d}_f, \quad J_f := \det \boldsymbol{F}_f, \qquad \boldsymbol{F}_s := \boldsymbol{I} + \nabla \boldsymbol{d}_s, \quad J_s := \det \boldsymbol{F}_s,$$

are defined similar to a total Lagrangian approach typical in solid mechanics. The fluid domain displacement is constructed via harmonic extension of $\boldsymbol{d}_s$ from $\hat{\Sigma}$ into $\hat{\Omega}_f$ via

$$-\Delta \boldsymbol{d}_f = 0 \qquad \text{in } \hat{\Omega}_f, \tag{2}$$

$$\boldsymbol{d}_f = \boldsymbol{d}_s \qquad \text{on } \hat{\Sigma}, \tag{3}$$

$$\boldsymbol{d}_f = \boldsymbol{0} \qquad \text{on } \hat{\Omega}_f \setminus \hat{\Sigma}, \tag{4}$$

which results in a sufficiently smooth map $\mathcal{A}_t(\boldsymbol{d}_f)$ from reference to current fluid domain. In the solid subdomain, the map $\mathcal{L}_t(\boldsymbol{d}_s)$ is directly constructed from the solid's displacement $\boldsymbol{d}_s$, governed by the balance of linear momentum in total Lagrangian form, written as

$$\rho_s \frac{\partial^2}{\partial t^2}\boldsymbol{d}_s - \nabla \cdot \boldsymbol{P} = \boldsymbol{0} \qquad \text{in } \hat{\Omega}_s, \tag{5}$$

$$\eta_s^R \frac{\partial}{\partial t}\boldsymbol{d}_s + \boldsymbol{P}\hat{\boldsymbol{n}}_s = \eta_s^R \boldsymbol{u}_f + J_f \boldsymbol{\sigma}_f \boldsymbol{F}_f^{-T} \hat{\boldsymbol{n}}_s \qquad \text{on } \hat{\Sigma}, \tag{6}$$

$$\boldsymbol{P}\hat{\boldsymbol{n}}_s = -k_e \boldsymbol{d}_s - c_e \frac{\partial}{\partial t}\boldsymbol{d}_s \qquad \text{on } \hat{\Gamma}_{R,s}, \tag{7}$$

$$\boldsymbol{d}_s = \boldsymbol{g}_s \qquad \text{on } \hat{\Gamma}_{D,s}, \tag{8}$$

where ρ_s is the solid's density, $\boldsymbol{P}$ the first Piola–Kirchhoff stress tensor, $\hat{\boldsymbol{n}}_s$ the unit outward normal on $\hat{\Omega}_s$, η_s^R is a Robin parameter, k_e and c_e are parameters to model viscoelastic support and $\boldsymbol{g}_s$ are Dirichlet data. Eq. (6) is a Robin condition defined on the interface, linearly combining the traction and velocity continuity conditions to improve convergence behaviour (see, e.g., [29,50,51]). The first Piola–Kirchhoff stress tensor of a quasi-incompressible, fibre-reinforced neo-Hookean solid is defined as [57]

$$\boldsymbol{P} := \mu_s J_s^{-2/3} \left(\boldsymbol{F}_s - \frac{1}{3} I_1 \boldsymbol{F}_s^{-T} \right) + \frac{\kappa_b}{2} \left(J_s^2 - 1 \right) \boldsymbol{F}_s^{-T} + \boldsymbol{F}_s \sum_{i=4,6} \left[2k_1 G_i \exp\left(k_2 G_i^2 \right) \frac{\partial G_i}{\partial \boldsymbol{C}} \right], \tag{9}$$

where we additionally introduce $G_i := J_s^{-2/3}\left[\kappa_c I_1 + (1-3\kappa_c)I_i\right] - 1$ for ease of notation and $\boldsymbol{C} := \boldsymbol{F}_s^T \boldsymbol{F}_s$, which yields

$$\frac{\partial G_i}{\partial \boldsymbol{C}} = J_s^{-2/3}\left\{\kappa_c \boldsymbol{I} + (1-3\kappa_c)\boldsymbol{A}_i - \frac{1}{3}\boldsymbol{C}^{-1}\left[\kappa_c I_1 + (1-3\kappa_c)I_i\right]\right\}.$$

Here, μ_s is the solid's shear rate, κ_s is the bulk modulus, k_1, k_2 and κ_c are (collagen) fibre parameters and the invariants $I_1 := \mathrm{tr}(\boldsymbol{C})$ and $I_i := \boldsymbol{C} : \boldsymbol{A}_i$, with $\boldsymbol{A}_i := \boldsymbol{m}_i \otimes \boldsymbol{m}_i$ and mean fibre directions $\boldsymbol{m}_i$, where the fibre contribution is active under tension only ($I_i > 1$) and zero otherwise. For later reference, we further provide relations for a standard quasi-incompressible neo-Hookean solid (10), the St. Venant–Kirchhoff model (11) and linear elasticity (12),

$$\boldsymbol{P} := \mu_s J_s^{-2/3}\left(\boldsymbol{F}_s - \frac{1}{3} I_1 \boldsymbol{F}_s^{-T}\right) + \frac{\kappa_b}{2}\left(J_s^2 - 1\right)\boldsymbol{F}_s^{-T} \tag{10}$$

$$\boldsymbol{P} := \lambda_s \boldsymbol{F}_s \mathrm{tr}\boldsymbol{E}_s + 2\mu_s \boldsymbol{F}_s \boldsymbol{E}_s, \quad \text{with} \quad \boldsymbol{E}_s := \frac{1}{2}\left(\boldsymbol{F}_s^T \boldsymbol{F}_s - \boldsymbol{I}\right) \tag{11}$$

$$\boldsymbol{P} := \lambda_s \boldsymbol{I} \nabla \cdot \boldsymbol{d}_s + \mu_s\left[\nabla \boldsymbol{d}_s + (\nabla \boldsymbol{d}_s)^T\right], \tag{12}$$

where λ_s and μ_s in Eqs. (11)–(12) are Lamé parameters. Adopting the ALE framework, the momentum and mass balance equations in the current fluid domain Ω_f^t read

$$\rho_f \frac{\partial}{\partial t}\boldsymbol{u}_f\Big|_{\mathcal{A}_t} + \rho_f \nabla \boldsymbol{u}_f\left(\boldsymbol{u}_f - \boldsymbol{u}_m\right) - \nabla \cdot \boldsymbol{\sigma}_f = \boldsymbol{0} \qquad \text{in } \Omega_f^t, \tag{13}$$

$$\nabla \cdot \boldsymbol{u}_f = 0 \qquad \text{in } \Omega_f^t, \tag{14}$$

$$\boldsymbol{u}_f = \frac{\partial}{\partial t}\boldsymbol{d}_s \qquad \text{on } \Sigma^t, \tag{15}$$

$$\boldsymbol{u}_f = \boldsymbol{g}_f \qquad \text{on } \Gamma_{D,f}^t, \tag{16}$$

$$\boldsymbol{\sigma}_f \boldsymbol{n}_f = \boldsymbol{t}_f \qquad \text{on } \Gamma_{N,f}^t, \tag{17}$$

with the fluid velocity $\boldsymbol{u}_f$ and pressure p_f, mesh velocity $\boldsymbol{u}_m := \frac{\partial}{\partial t}\boldsymbol{d}_f\big|_{\mathcal{A}_t}$, $\frac{\partial}{\partial t}\cdot\big|_{\mathcal{A}_t}$ denoting the ALE time derivative and boundary data $\boldsymbol{g}_f$ and $\boldsymbol{t}_f$ on the respective boundary segments. On the interface, a pure Dirichlet condition expressed via the solid's material velocity $\frac{\partial}{\partial t}\boldsymbol{d}_s$ is enforced, leading to a Dirichlet–Robin coupling algorithm. The stress tensor for a generalised Newtonian fluid is

$$\boldsymbol{\sigma}_f := -p_f \boldsymbol{I} + 2\mu_f \nabla^{\mathrm{S}} \boldsymbol{u}_f, \tag{18}$$

with the fluid's local viscosity μ_f depending on the shear rate $\dot{\gamma}$,

$$\dot{\gamma} := \sqrt{\frac{1}{2}\nabla^{\mathrm{S}}\boldsymbol{u}_f : \nabla^{\mathrm{S}}\boldsymbol{u}_f},$$

and $\nabla^{\mathrm{S}}\boldsymbol{u}_f := \frac{1}{2}\left[\nabla \boldsymbol{u}_f + \left(\nabla \boldsymbol{u}_f\right)^T\right]$ being the symmetric velocity gradient. The inhomogeneous viscosity allows incorporating shear-thickening or shear-thinning effects, e.g., via [58]

$$\eta(\dot{\gamma}) := \eta_\infty + (\eta_0 - \eta_\infty)\left[\kappa_f + \left(\lambda_f \dot{\gamma}\right)^a\right]^{\frac{\xi-1}{a}}, \tag{19}$$

where η_0 and η_∞ are upper and lower viscosity limits and κ_f, λ_f, a and ξ are fitting parameters.

System (13)–(17) can be reformulated through the pressure Poisson equation [52,59]

$$-\Delta p_f = \nabla \cdot\left[\rho_f \nabla \boldsymbol{u}_f\left(\boldsymbol{u}_f - \boldsymbol{u}_m\right) - 2\nabla^{\mathrm{S}}\boldsymbol{u}_f \nabla \mu_f\right] + \left[\nabla \times \left(\nabla \times \boldsymbol{u}_f\right)\right] \cdot \nabla \mu_f \qquad \text{in } \Omega_f^t \tag{20}$$

and fully consistent Dirichlet and Neumann boundary conditions

$$p_f = -\mu_f \nabla \cdot \boldsymbol{u}_f + \boldsymbol{n}_f \cdot \left(2\mu_f \nabla^{\mathrm{S}}\boldsymbol{u}_f \boldsymbol{n}_f - \boldsymbol{t}_f\right) \qquad \text{on } \Gamma_{N,f}^t, \tag{21}$$

$$\boldsymbol{n}_f \cdot \nabla p_f = -\rho_f \boldsymbol{n}_f \cdot \left[\frac{\partial}{\partial t}\boldsymbol{g}_f\Big|_{\mathcal{A}_t} + \nabla \boldsymbol{u}_f\left(\boldsymbol{u}_f - \boldsymbol{u}_m\right)\right] - \mu_f \boldsymbol{n}_f \cdot \left[\nabla \times \left(\nabla \times \boldsymbol{u}_f\right)\right] + 2\boldsymbol{n}_f \cdot \left(\nabla^{\mathrm{S}}\boldsymbol{u}_f \nabla \mu_f\right) \qquad \text{on } \Gamma_{D,f}^t, \tag{22}$$

Table 1
Parameters in the generalised-α time integration scheme for Newmark-β [61], HHT-α [62], WBZ-α [63] and CH-α [64] time integration.

	Newmark-β	HHT-α	WBZ-α	CH-α
α_m	0	0	$\frac{\rho_\infty - 1}{1+\rho_\infty}$	$\frac{2\rho_\infty - 1}{1+\rho_\infty}$
α_f	0	$\frac{1-\rho_\infty}{1+\rho_\infty}$	0	$\frac{\rho_\infty}{1+\rho_\infty}$

replacing Eqs. (16) and (17), and an analogous interface condition

$$\boldsymbol{n}_f \cdot \nabla p_f = -\rho_f \boldsymbol{n}_f \cdot \left[\frac{\partial^2}{\partial t^2} \boldsymbol{d}_s + \nabla \boldsymbol{u}_f \left(\boldsymbol{u}_f - \boldsymbol{u}_m \right) \right] - \mu_f \boldsymbol{n}_f \cdot \left[\nabla \times \left(\nabla \times \boldsymbol{u}_f \right) \right] + 2 \boldsymbol{n}_f \cdot \left(\nabla^\mathrm{S} \boldsymbol{u}_f \nabla \mu_f \right) \qquad \text{on } \Sigma^t, \tag{23}$$

merely replacing $\frac{\partial}{\partial t} \boldsymbol{u}_f \big|_{\mathcal{A}_t}$ by the solid's material acceleration. Note that the pressure Dirichlet condition (21) involves discontinuous data, while the pressure itself is continuous. For this reason, we introduce an intermediate variable ζ and perform an L^2-projection of the boundary data onto a continuous space defined on $\Gamma^t_{N,f}$. An in-depth discussion on consistent PPE-based solvers can be found in our recent work [52]; here, we restrict ourselves to the Robin interface condition for the solid subproblem (6). The fluid subproblem, however, treats the interface as a Dirichlet boundary, enforcing $\boldsymbol{u}_f = \frac{\partial}{\partial t} \boldsymbol{d}_s$, which then leads to Eq. (23) in the split-step scheme.

The mass conservation and temporal stability of this split-step scheme are further improved via Leray projection:

$$\begin{aligned} -\Delta \psi &= -\nabla \cdot \boldsymbol{u}_f && \text{in } \Omega^t_f, \\ \boldsymbol{n}_f \cdot \nabla \psi &= 0 && \text{on } \Gamma^t_{D,f} \cup \Sigma^t, \\ \psi &= 0 && \text{on } \Gamma^t_{N,f}, \end{aligned}$$

to recover a weakly divergence-free velocity $\check{\boldsymbol{u}}_f := \boldsymbol{u}_f - \nabla \psi$. Following [59,60], we employ so-called divergence damping, which acts on past velocities only, thus preserving velocity boundary conditions and sparing a vector-valued velocity projection step.

Discretising in time, we decompose the interval $(0, T]$ into N_t steps of possibly variable size $\Delta t^n = t^{n+1} - t^n$, $n = 0, \ldots, N_t$ and apply generalised-α time integration for the structural problem

$$\rho_s \left(\alpha'_\mathrm{m} \ddot{\boldsymbol{d}}_s^{n+1} + \alpha_\mathrm{m} \ddot{\boldsymbol{d}}_s^{n} \right) - \alpha'_\mathrm{f} \nabla \cdot \boldsymbol{P} \left(\boldsymbol{d}_s^{n+1} \right) - \alpha_\mathrm{f} \nabla \cdot \boldsymbol{P} \left(\boldsymbol{d}_s^{n} \right) = \boldsymbol{0} \qquad \text{in } \hat{\Omega}_s, \tag{24}$$

where the structure's accelerations $\ddot{\boldsymbol{d}}_s$ and velocities $\dot{\boldsymbol{d}}_s$ are [61]

$$\ddot{\boldsymbol{d}}_s^{n+1} = \frac{1}{\beta \Delta t^2} \left(\boldsymbol{d}_s^{n+1} - \boldsymbol{d}_s^{n} \right) - \frac{1}{\beta \Delta t} \dot{\boldsymbol{d}}_s^{n} + \left(1 - \frac{1}{2\beta} \right) \ddot{\boldsymbol{d}}_s^{n} \tag{25}$$

$$\dot{\boldsymbol{d}}_s^{n+1} = \frac{\gamma}{\beta \Delta t} \left(\boldsymbol{d}_s^{n+1} - \boldsymbol{d}_s^{n} \right) - \left(1 - \frac{\gamma}{\beta} \right) \dot{\boldsymbol{d}}_s^{n} + \Delta t \left(1 - \frac{\gamma}{2\beta} \right) \ddot{\boldsymbol{d}}_s^{n}, \tag{26}$$

$\alpha'_\mathrm{m} = 1 - \alpha_\mathrm{m}$ and $\alpha'_\mathrm{f} = 1 - \alpha_\mathrm{f}$ with time integration parameters $\gamma = \frac{1}{2} - \alpha_\mathrm{m} + \alpha_\mathrm{f}$ and $\beta = \frac{1}{4} \left(1 - \alpha_\mathrm{m} + \alpha_\mathrm{f} \right)^2$ and α_f and α_m depending on the spectral radius in the high frequency limit ρ_∞ according to Table 1. For the fluid subproblem, we employ backward differentiation formulae (BDF) of order m,

$$\frac{\partial}{\partial t} \boldsymbol{u}_f \Big|_{\mathcal{A}_t} \approx \sum_{j=0}^{m} \alpha_j^m \boldsymbol{u}_f^{n+1-j},$$

or, when including contributions from divergence damping,

$$\frac{\partial}{\partial t} \boldsymbol{u}_f \Big|_{\mathcal{A}_t} \approx \alpha_0^m \boldsymbol{u}_f^{n+1} + \sum_{j=0}^{m-1} \alpha_{j+1}^m \left(\boldsymbol{u}_f^{n-j} - \nabla \psi^{n-j} \right). \tag{27}$$

Table 2
Coefficients for BDF schemes, α_j^m, and extrapolation, β_j^m [65].

	Order $m=1$		Order $m=2$		
j	0	1	0	1	2
α_j^m	$\frac{1}{\Delta t^n}$	$-\frac{1}{\Delta t^n}$	$\frac{2\Delta t^n+\Delta t^{n-1}}{\Delta t^n(\Delta t^n+\Delta t^{n-1})}$	$-\frac{\Delta t^n+\Delta t^{n-1}}{\Delta t^n \Delta t^{n-1}}$	$\frac{\Delta t^n}{\Delta t^{n-1}(\Delta t^n+\Delta t^{n-1})}$
β_j^m	$\times$	1	$\times$	$1+\frac{\Delta t^n}{\Delta t^{n-1}}$	$\frac{\Delta t^n}{\Delta t^{n-1}}$

Also, we employ extrapolations from previous time steps of the same order m, as shown for the pressure p_f:

$$p_f^{n+1} \approx p_f^\star = \sum_{j=1}^{m} \beta_j^m p_f, \tag{28}$$

with coefficients α_j^m and β_j^m listed in Table 2. Then, the semi-implicit coupling algorithm iterates solely on the fluid pressure and solid displacements until absolute and relative convergence criteria,

$$\left\| p_f^{k+1}|_{\Sigma^t} - p_f^k|_{\Sigma^t} \right\| < \epsilon_{\text{abs}}^p, \quad \left\| p_f^{k+1}|_{\Sigma^t} - p_f^k|_{\Sigma^t} \right\| < \epsilon_{\text{rel}}^p \left\| p_f^{k+1}|_{\Sigma^t} \right\|, \tag{29}$$

are reached for the fluid pressure p_f and for the solid displacement $\boldsymbol{d}_s$,

$$\left\| \boldsymbol{d}_s^{k+1}|_{\hat{\Sigma}} - \boldsymbol{d}_s^k|_{\hat{\Sigma}} \right\| < \epsilon_{\text{abs}}^d, \quad \left\| \boldsymbol{d}_s^{k+1}|_{\hat{\Sigma}} - \boldsymbol{d}_s^k|_{\hat{\Sigma}} \right\| < \epsilon_{\text{rel}}^d \left\| \boldsymbol{d}_s^{k+1}|_{\hat{\Sigma}} \right\|, \tag{30}$$

with problem-dependent tolerances ϵ_{abs}^p, ϵ_{rel}^p, ϵ_{abs}^d and ϵ_{rel}^d. Then, the semi-implicit Dirichlet–Robin (SIDR) variant of the coupling algorithm [52] reads as follows: Given the past time step's solution $\boldsymbol{d}_f^n$, $\boldsymbol{d}_s^n$, $\boldsymbol{u}_f^n$, p_f^n, μ_f^n, $\dot{\boldsymbol{d}}_s^n$, $\ddot{\boldsymbol{d}}_s^n$ and additionally $\boldsymbol{d}_f^{n-1}$, $\boldsymbol{d}_s^{n-1}$, $\boldsymbol{u}_f^{n-1}$, p_f^{n-1}, μ_f^{n-1} for second-order extrapolation and BDF schemes, perform the steps listed in Eqs. (31)–(39) at each time step n.

---

1. *Extrapolation and initial guess:* Compute extrapolations $\boldsymbol{d}_s^\star$, $\mu_f^\star$, $\boldsymbol{u}_f^\star$ and $p_f^\star$ (28) and set as initial guess

$$\boldsymbol{d}_s^k = \boldsymbol{d}_s^\star, \quad \text{and} \quad p_f^k = p_f^\star. \tag{31}$$

2. *Mesh motion:* Update the fluid domain Ω_f^t based on the extrapolated structural displacement $\boldsymbol{d}_s^\star$, i.e., find $\boldsymbol{d}_f^{n+1} \in [H^1(\hat{\Omega}_f)]^d$ such that $\boldsymbol{d}_f|_{\hat{\Sigma}} = \boldsymbol{d}_s^\star$ and $\boldsymbol{d}_f|_{\partial\hat{\Omega}_f \setminus \hat{\Sigma}} = \boldsymbol{0}$ and

$$\left\langle \nabla\boldsymbol{\varphi}, \nabla\boldsymbol{d}_f^{k+1} \right\rangle_{\hat{\Omega}_f} = 0 \qquad \forall \boldsymbol{\varphi} \in [H^1(\hat{\Omega}_f)]^d, \text{ with } \boldsymbol{\varphi}|_{\partial\hat{\Omega}_f} = \boldsymbol{0}, \tag{32}$$

and compute the mesh velocity $\boldsymbol{u}_m = \frac{\partial}{\partial t}\boldsymbol{d}_f\big|_{\mathcal{A}_t}$ via the BDF scheme (27).

3. *Viscosity projection:* Find the viscosity $\mu_f^{n+1} \in H^1(\Omega_f^t)$ based on the extrapolated velocity $\boldsymbol{u}_f^\star$, such that

$$\left\langle \varphi, \mu_f^{n+1} \right\rangle_{\Omega_f^t} = \left\langle \varphi, \eta\left(\dot{\gamma}(\nabla\boldsymbol{u}_f^\star)\right) \right\rangle_{\Omega_f^t} \qquad \forall \varphi \in L^2(\Omega_f^t). \tag{33}$$

4. *Pressure boundary condition:* Project the pressure Dirichlet data using an intermediate variable ζ,

$$\zeta = -\mu_f^{n+1}\nabla\cdot\boldsymbol{u}_f^\star + \boldsymbol{n}_f \cdot \left(2\mu_f^{n+1}\nabla^{\text{S}}\boldsymbol{u}_f^\star\boldsymbol{n}_f - \boldsymbol{t}_f^{n+1}\right) \qquad \text{on } \Gamma_{N,f}^t. \tag{34}$$

5. *Pressure/structure coupling:*
WHILE not converged according to Eqs. (29)–(30) **DO**

(a) *PPE:* Find $p_f^{k+1} \in H^1(\Omega_f^t)$, such that $p_f^{k+1}|_{\Gamma_{N,f}^t} = \zeta$ and

$$\begin{aligned}\left\langle \nabla\varphi, \nabla p_f^{k+1} \right\rangle_{\Omega_f^t} = \left\langle \nabla\varphi, 2\left(\nabla\boldsymbol{u}_f^\star\right)^T \nabla\mu_f^{n+1} - \rho_f\nabla\boldsymbol{u}_f^\star\left(\boldsymbol{u}_f^\star - \boldsymbol{u}_m\right) \right\rangle_{\Omega_f^t} - \left\langle \varphi\boldsymbol{n}_f, \rho_f \sum_{j=0}^{m} \alpha_j^m \boldsymbol{g}_f^{n+1-j} \right\rangle_{\Gamma_{D,f}^t} \\ - \left\langle \varphi\boldsymbol{n}_f, \rho_f\ddot{\boldsymbol{d}}_s^{n+1} \right\rangle_{\Sigma^t} + \left\langle \boldsymbol{n}_f \times \nabla\varphi, \mu_f^{n+1}\nabla\times\boldsymbol{u}_f^\star \right\rangle_{\Sigma^t \cup \Gamma_{D,f}^t}\end{aligned} \tag{35}$$

holds for all $\varphi \in H^1(\Omega_f^t)$, where $\varphi|_{\Gamma_{N,f}^t} = 0$ and $\ddot{\boldsymbol{d}}_s^{n+1}$ is evaluated using the last iterate $\boldsymbol{d}_s^k$ in Eq. (25).

(b) *Solid momentum:* Find $\boldsymbol{d}_s^{k+1} \in [H^1(\hat{\Omega}_s)]^d$ with $\boldsymbol{d}_s^{k+1}|_{\hat{\Gamma}_{D,s}} = \boldsymbol{g}_s^{n+1}$, such that for all $\boldsymbol{\varphi} \in [H^1(\hat{\Omega}_s)]^d$ with $\boldsymbol{\varphi}|_{\hat{\Gamma}_{D,s}} = \boldsymbol{0}$ there holds:

$$\begin{aligned} &\rho_s \left\langle \boldsymbol{\varphi}, \alpha_{\mathrm{m}}' \ddot{\boldsymbol{d}}_s^{n+1} + \alpha_{\mathrm{m}} \ddot{\boldsymbol{d}}_s^{n} \right\rangle_{\hat{\Omega}_s} + \left\langle \nabla \boldsymbol{\varphi}, \alpha_{\mathrm{f}}' \boldsymbol{P}(\boldsymbol{d}_s^{k+1}) + \alpha_{\mathrm{f}} \boldsymbol{P}(\boldsymbol{d}_s^{n}) \right\rangle_{\hat{\Omega}_s} \\ &= \alpha_{\mathrm{f}} \left\langle \boldsymbol{\varphi}, \boldsymbol{P}(\boldsymbol{d}_s^{n}) \hat{\boldsymbol{n}}_s \right\rangle_{\hat{\Gamma}_{R,s} \cup \hat{\Sigma}} - \alpha_{\mathrm{f}}' \left\langle \boldsymbol{\varphi}, k_e \boldsymbol{d}_s^{k+1} + c_e \dot{\boldsymbol{d}}_s^{n+1} \right\rangle_{\hat{\Gamma}_{R,s}} \\ &\quad + \alpha_{\mathrm{f}}' \left\langle \boldsymbol{\varphi}, \eta_s^R \left(\boldsymbol{u}_f^{\star} - \dot{\boldsymbol{d}}_s^{n+1} \right) + J_f \boldsymbol{\sigma}_f \left(\boldsymbol{u}_f^{\star}, p_f^{k+1}, \mu_f^{n+1} \right) \boldsymbol{F}_f^{-T} \hat{\boldsymbol{n}}_s \right\rangle_{\hat{\Sigma}}, \end{aligned} \tag{36}$$

where $\ddot{\boldsymbol{d}}_s^{n+1}$ and $\dot{\boldsymbol{d}}_s^{n+1}$ are evaluated with $\boldsymbol{d}_s^{k+1}$, which is a nonlinear problem to be solved with, e.g., Newton's method.

(c) Apply an acceleration scheme like Aitken's method or IQN-ILS on the structure's displacement on the interface $\boldsymbol{d}_{\hat{\Sigma}}$ (see Section 3.3), i.e., set

$$\boldsymbol{d}_s^{k+1}|_{\hat{\Sigma}} = \boldsymbol{d}_{\hat{\Sigma}}^{k+1} \left(\boldsymbol{d}_s^{k+1}, \boldsymbol{d}_s^{k}, \dots \right), \tag{37}$$

and update iterates $\boldsymbol{d}_s^k = \boldsymbol{d}_s^{k+1}$ and $p_f^k = p_f^{k+1}$.
END DO

6. *Update converged iterates:* Set $\boldsymbol{d}_s^{n+1} = \boldsymbol{d}_s^{k+1}$ and $p_f^{n+1} = p_f^{k+1}$.
7. *Fluid momentum:* Find $\boldsymbol{u}_f^{n+1} \in [H^1(\Omega_f^t)]^d$ with $\boldsymbol{u}_f^{n+1} = \boldsymbol{g}_f^{n+1}$ on $\Gamma_{D,f}^t$, $\boldsymbol{u}_f^{n+1} = \dot{\boldsymbol{d}}_s^{n+1}$ on Σ^t, such that

$$\begin{aligned} &\rho_f \left\langle \boldsymbol{\varphi}, \alpha_o^m \boldsymbol{u}_f^{n+1} + \nabla \boldsymbol{u}_f^{n+1} \left(\boldsymbol{u}_f^{\star} - \boldsymbol{u}_m \right) \right\rangle_{\Omega_f^t} + \left\langle \nabla \boldsymbol{\varphi}, 2\mu_f^{n+1} \nabla^{\mathrm{S}} \boldsymbol{u}_f^{n+1} \right\rangle_{\Omega_f^t} \\ &= \left\langle \nabla \boldsymbol{\varphi}, p_f^{n+1} \boldsymbol{I} \right\rangle_{\Omega_f^t} - \rho_f \left\langle \boldsymbol{\varphi}, \sum_{j=0}^{m-1} \alpha_{j+1}^m \left(\boldsymbol{u}_f^{n-j} - \nabla \psi^{n-j} \right) \right\rangle_{\Omega_f^t} + \left\langle \boldsymbol{\varphi}, \boldsymbol{t}_f^{n+1} \right\rangle_{\Gamma_{N,f}^t} \end{aligned} \tag{38}$$

for all $\boldsymbol{\varphi} \in [H^1(\Omega_f^t)]^d$, with $\boldsymbol{\varphi} = \boldsymbol{0}$ on $\Gamma_{D,f}^t \cup \Sigma^t$, where the auxiliary projection variable ψ is considered only for the past time steps' velocities.

8. *Divergence damping:* Update the projection variable $\psi^{n+1} \in H^1(\Omega_f^t)$ via $\boldsymbol{u}_f^{n+1}$, s. t. $\psi^{n+1}|_{\Gamma_{N,f}^t} = 0$ and

$$\left\langle \nabla \varphi, \nabla \psi^{n+1} \right\rangle_{\Omega_f^t} = -\left\langle \varphi, \nabla \cdot \boldsymbol{u}_f^{n+1} \right\rangle_{\Omega_f^t} \qquad \forall \varphi \in H^1(\Omega_f^t),\ \varphi|_{\Gamma_{N,f}^t} = 0, \tag{39}$$

to be used as ψ^n in the next time step.

3. Numerical techniques

The SIDR scheme (31)–(39) as proposed by the authors [52] serves well as a starting point for tackling biomedical applications. As is well known in such scenarios, problems arise as the Reynolds number increases, fluid is entering over Neumann boundaries or the added-mass effect becomes dominant. Standard remedies can be incorporated in the present semi-implicit framework, but care must be taken to preserve consistency and stability. The following extensions of and improvements to the original SIDR scheme [52] are novel contributions of the present work. Here, we adapt well-trusted concepts as remedies to specific numerical problems within the SIDR framework and maintain the advantages regarding flexibility, generality and robustness.

3.1. Backflow stabilisation

In many flow simulations, outflow boundaries are defined where the fluid is assumed to exit the computational domain. On these boundaries, Neumann conditions are enforced to set a reference pressure. Already for moderate Reynolds numbers of say, $\mathrm{Re} = \mathcal{O}(500)$ – as often encountered in haemodynamics or the respiratory context – this approach can lead to severe instabilities if the flow is reversed, entering from the exterior of the considered domain.

An effective remedy for such effects is backflow stabilisation [53], where one modifies the Cauchy traction to

$$\boldsymbol{t}_f = \boldsymbol{\sigma}_f \boldsymbol{n}_f + \alpha_b \frac{\rho}{2} \boldsymbol{u}_f (\boldsymbol{u}_f \cdot \boldsymbol{n}_f)_-, \quad \text{with} \quad (\boldsymbol{u}_f \cdot \boldsymbol{n}_f)_- = \begin{cases} -\boldsymbol{u}_f \cdot \boldsymbol{n}_f & \text{for } \boldsymbol{u}_f \cdot \boldsymbol{n}_f < 0, \\ 0 & \text{otherwise,} \end{cases} \tag{40}$$

and a parameter $\alpha_b \geq 1$, within this work simply chosen as $\alpha_b = 1$. Note also that the stabilisation term is only contributing when fluid is entering over the outflow boundary and zero for outward flow.

This modified traction naturally enters the fluid momentum balance equation (38), but is also considered in the projection of the pressure Dirichlet data on $\Gamma^t_{N,f}$ (34). As this critical term is non-zero depending on the local flow field, it is "switched on" abruptly, which is bound to cause trouble, as will be demonstrated in Section 5. Nonetheless, it prevents divergence of the solver, but heavily influences the actually enforced traction on the boundary. Of particular importance is consistency between the fluid's momentum balance equation and the PPE — these two steps consider backflow stabilisation based on the extrapolated velocity $\boldsymbol{u}^\star_f$, activating the stabilisation at the same time. Then, the added boundary term can be considered semi-implicitly in the fluid momentum balance equation, adding $\left\langle \boldsymbol{\varphi}, \rho_f \boldsymbol{u}_f^{n+1} (\boldsymbol{u}^\star_f \cdot \boldsymbol{n}_f)_- \right\rangle_{\Gamma^t_{N,f}}$ to the left-hand side.

3.2. Stabilising convective effects

The Galerkin finite element formulation of the fluid's momentum balance equation is known to suffer from spurious oscillations for high Reynolds numbers and coarse meshes. Although our split-step scheme does not necessarily assume a finite element discretisation of the fluid momentum step, we herein do use finite elements to discretise all unknowns. Thus, we will demonstrate how standard techniques to suppress the arising instabilities can be incorporated. A well-established residual-based method often resorted to in this context is the Galerkin least-squares stabilisation [54]. Velocity and pressure are split on the (spatially) continuous level, such that it suffices to modify the weak form of the fluid momentum equation (38), adding

$$\left\langle \tau_e \mathrm{L}(\boldsymbol{\varphi}), \mathrm{R}(\boldsymbol{u}_f^{n+1}) \right\rangle_{\Omega^t_{f,e}} \tag{41}$$

to the left-hand side in an element-wise manner as indicated by $\Omega^t_{f,e}$. Here, $\mathrm{R}(\boldsymbol{u}_f^{n+1})$ is the residual of the time-discrete strong form

$$\begin{aligned} \mathrm{R}(\boldsymbol{u}_f^{n+1}) \coloneqq\ & \rho_f \alpha_0^m \boldsymbol{u}_f^{n+1} + \rho_f \sum_{j=0}^{m-1} \alpha_{j+1}^m \left(\boldsymbol{u}_f^{n-j} - \nabla \psi^{n-j} \right) + \nabla p_f^{n+1} \\ & + \rho_f \nabla \boldsymbol{u}_f^{n+1} \left(\boldsymbol{u}^\star_f - \boldsymbol{u}_m \right) - \mu_f^{n+1} \nabla (\nabla \cdot \boldsymbol{u}_f) - \mu_f^{n+1} \Delta \boldsymbol{u}_f^{n+1} - 2 \nabla^{\mathrm{S}} \boldsymbol{u}_f^{n+1} \nabla \mu_f^{n+1}, \end{aligned}$$

$\mathrm{L}(\boldsymbol{\varphi})$ is the corresponding operator, given as

$$\mathrm{L}(\boldsymbol{\varphi}) \coloneqq\ \rho_f \alpha_0^m \boldsymbol{\varphi} + \rho_f \nabla \boldsymbol{\varphi} \left(\boldsymbol{u}^\star_f - \boldsymbol{u}_m \right) - \mu_f^{n+1} \nabla (\nabla \cdot \boldsymbol{\varphi}) - \mu_f^{n+1} \Delta \boldsymbol{\varphi} - 2 \nabla^{\mathrm{S}} \boldsymbol{\varphi} \nabla \mu_f^{n+1},$$

and τ_e is the stabilisation parameter, defined as [66]

$$\tau_e \coloneqq \xi(\iota) \frac{1}{\rho_f} \left[\left(\frac{2}{\Delta t^n} \right)^2 + \left(\frac{2}{h_e} \left\| \boldsymbol{u}^\star_f - \boldsymbol{u}_m \right\| \right)^2 + \left(\frac{4 \mu_f^{n+1}}{\rho_f h_e^2} \right)^2 \right]^{-\frac{1}{2}},$$

with the element size $h_e \coloneqq \left| \Omega_{f,e} \right|^{\frac{1}{d}}$ and an additional scaling parameter $\xi(\iota)$,

$$\xi(\iota) \coloneqq \begin{cases} \frac{\iota}{3} & \text{for } \iota < 3, \\ 1 & \text{otherwise,} \end{cases} \quad \text{and} \quad \iota \coloneqq \frac{\rho_f \left\| \nabla \boldsymbol{u}^\star_f \left(\boldsymbol{u}^\star_f - \boldsymbol{u}_m \right) \right\| h_e^2}{4 \mu_f^{n+1} \left\| \boldsymbol{u}^\star_f \right\|}.$$

Note that we linearise τ_e by evaluating it with $\boldsymbol{u}^\star_f$ and the stabilisation vanishes as $h_e \to 0$, $\Delta t \to 0$, ensuring consistency. Dominant convection renders the viscous contribution less important in this scenario, such that we accept an inviscid residual — in the context of inf-sup stabilisation, however, this can lead to numerical artifacts (cf. [67,68]). Using lower-order shape functions, the residual is incomplete, but reaction and convection terms

dominate over vanishing diffusion terms, which causes instabilities in convective regions initially. In areas where the local Reynolds number is much lower and viscous stresses are important, the additional scaling via $\xi(\iota)$ mitigates the errors otherwise introduced by the incomplete residual in GLS stabilisation.

3.3. Accelerating partitioned FSI schemes

To decrease the number of iterations needed in the SIDR scheme, techniques using the individual field solvers as black boxes are conveniently applied in addition to Robin interface conditions. To this end, reinterpret the pressure/structure coupling loop as a fixed-point iteration in the interface displacement $\boldsymbol{d}^k_{\hat{\Sigma}} := \boldsymbol{d}^k_s|_{\hat{\Sigma}}$, $\boldsymbol{d}^k_{\hat{\Sigma}} \in \mathbb{R}^{N_{\hat{\Sigma}}\times 1}$, with $N_{\hat{\Sigma}}$ being the number of displacement degrees of freedom on the interface. A single iteration of the pressure/structure coupling loop consists of the PPE step (35) and a structure displacement solve (36), such that we can write the update as

$$\tilde{\boldsymbol{d}}^k_{\hat{\Sigma}} := \mathrm{S} \circ \mathrm{P}\left(\boldsymbol{d}^k_{\hat{\Sigma}}\right), \tag{42}$$

where S and P denote the corresponding pressure and structure displacement interface operators. The residual $\boldsymbol{r}^k$ of this interface equation is thus

$$\boldsymbol{r}^k := \mathrm{S} \circ \mathrm{P}\left(\boldsymbol{d}^k_{\hat{\Sigma}}\right) - \boldsymbol{d}^k_{\hat{\Sigma}} = \tilde{\boldsymbol{d}}^k_{\hat{\Sigma}} - \boldsymbol{d}^k_{\hat{\Sigma}}\,. \tag{43}$$

A straightforward approach to accelerate convergence is to introduce a fixed relaxation factor ω, usually chosen in the range $0 < \omega < 1$, and modify the interface displacement according to

$$\boldsymbol{d}^{k+1}_{\hat{\Sigma}} = \omega\,\tilde{\boldsymbol{d}}^k_{\hat{\Sigma}} + (1-\omega)\,\boldsymbol{d}^k_{\hat{\Sigma}}.$$

An equally elementary, yet powerful – hence very popular – option is Aitken's method, which defines a dynamic relaxation parameter ω_k in a recursive manner [28]:

$$\omega_k = -\omega_{k-1}\left\|\Delta\boldsymbol{r}^k\right\|^{-2}\boldsymbol{r}^{k-1}\cdot\Delta\boldsymbol{r}^k, \quad \text{with} \quad \Delta\boldsymbol{r}^k = \boldsymbol{r}^k - \boldsymbol{r}^{k-1}. \tag{44}$$

Alternatively, the IQN-ILS scheme [33,69] approximates a step of Newton's method applied to Eq. (43), using residuals and solution vectors obtained in previous time steps and iterations via

$$\boldsymbol{d}^{k+1}_{\hat{\Sigma}} = \tilde{\boldsymbol{d}}^k_{\hat{\Sigma}} - \left(\left.\frac{\partial\boldsymbol{r}}{\partial\boldsymbol{d}_{\hat{\Sigma}}}\right|_{\boldsymbol{d}^k_{\hat{\Sigma}}}\right)^{-1}\boldsymbol{r}^k \approx \tilde{\boldsymbol{d}}^k_{\hat{\Sigma}} + \mathbf{W}\boldsymbol{c}, \tag{45}$$

where the columns of $\mathbf{W} \in \mathbb{R}^{N_{\hat{\Sigma}}\times k}$ hold differences of the unmodified interface displacement vectors given as

$$\mathbf{W} = \left(\Delta\tilde{\boldsymbol{d}}^k_{\hat{\Sigma}}, \Delta\tilde{\boldsymbol{d}}^{k-1}_{\hat{\Sigma}}, \ldots, \Delta\tilde{\boldsymbol{d}}^1_{\hat{\Sigma}}\right), \quad \text{with} \quad \Delta\tilde{\boldsymbol{d}}^k_{\hat{\Sigma}} = \tilde{\boldsymbol{d}}^k_{\hat{\Sigma}} - \tilde{\boldsymbol{d}}^{k-1}_{\hat{\Sigma}} \tag{46}$$

and the coefficient vector $\boldsymbol{c} \in \mathbb{R}^{k\times 1}$ is the solution to the least-squares problem

$$\min_{\boldsymbol{c}}\left\|\mathbf{V}\boldsymbol{c} + \boldsymbol{r}^k\right\|, \quad \text{with} \quad \mathbf{V} = \left(\Delta\boldsymbol{r}^k, \Delta\boldsymbol{r}^{k-1}, \ldots, \Delta\boldsymbol{r}^1\right) \in \mathbb{R}^{N_{\hat{\Sigma}}\times k}. \tag{47}$$

This minimisation problem is solved via QR decomposition, $\mathbf{V} = \mathbf{QR}$, appending and deleting columns from $\mathbf{V}$ and updating the decomposition accordingly. Only the small upper triangular matrix $\mathbf{R} \in \mathbb{R}^{k\times k}$ is stored, while the action of the orthogonal matrix $\mathbf{Q} \in \mathbb{R}^{N_{\hat{\Sigma}}\times k}$ onto $\boldsymbol{r}^k$ is reformulated as

$$\mathbf{Q}^T\boldsymbol{r}^k = \mathbf{R}^{-T}\mathbf{V}^T\boldsymbol{r}^k.$$

Then, two ingredients are combined to further improve performance and numerical stability [69]: (i) data pairs from q previous time steps are re-used, but individual difference vectors $\Delta\tilde{\boldsymbol{d}}^k_{\hat{\Sigma}}$ and $\Delta\boldsymbol{r}^k$ must not span different time levels, and (ii) while updating the QR decomposition, linearly dependent columns in $\mathbf{V}$ are detected by $\mathbf{R}_{kk} < \epsilon_{\mathrm{QR}}$, rejected, and removed from the data matrices $\mathbf{V}$ and $\mathbf{W}$. The IQN-ILS-accelerated pressure/structure coupling loop as a part of the SIDR scheme is summarised in Algorithm 1.

This simple filtering approach, rejecting columns which otherwise lead to small diagonal values in $\mathbf{R}$, is found rather robust. Moreover, implicitly computing $\mathbf{Q}^T\boldsymbol{r}^k$ by an additional back-insertion pass on $\mathbf{R}^T$ is uncritical in the

Algorithm 1 IQN-ILS-accelerated pressure/structure coupling

$k = 0$
while Not converged acc. to Eqs. (29)–(30) **do**
  Perform single coupling step: $\tilde{\boldsymbol{d}}^k_{\hat{\Sigma}} = \mathrm{S} \circ \mathrm{P}\left(\boldsymbol{d}^k_{\hat{\Sigma}}\right)$
  Remove columns from $\mathbf{V}$ and $\mathbf{W}$ corresponding to time step $n - q - 1$
  Update residual: $\boldsymbol{r}^k = \tilde{\boldsymbol{d}}^k_{\hat{\Sigma}} - \boldsymbol{d}^k_{\hat{\Sigma}}$
  Update difference vectors: $\Delta\tilde{\boldsymbol{d}}^k_{\hat{\Sigma}} = \tilde{\boldsymbol{d}}^k_{\hat{\Sigma}} - \tilde{\boldsymbol{d}}^{k-1}_{\hat{\Sigma}}$ and $\Delta\boldsymbol{r}^k = \boldsymbol{r}^k - \boldsymbol{r}^{k-1}$
  Insert new data pairs into $\mathbf{V}$ and $\mathbf{W}$ as defined in (46) and (47)
  if $k = 0$ and ($q = 0$ or $n = 0$) **then**
    Initial relaxation step: $\boldsymbol{d}^{k+1}_{\hat{\Sigma}} = \omega\,\tilde{\boldsymbol{d}}^k_{\hat{\Sigma}} + (1-\omega)\,\boldsymbol{d}^k_{\hat{\Sigma}}$
  else
    Update QR decomposition, add column k if $\mathbf{R}_{kk} \geq \epsilon_{\mathrm{QR}}$
    Remove columns from $\mathbf{V}$ and $\mathbf{W}$ that were rejected
    Compute $-\mathbf{Q}^T\boldsymbol{r}^k$ by solving $\mathbf{R}^T\boldsymbol{b} = -\boldsymbol{a}$ with $\boldsymbol{a} = \mathbf{V}^T\boldsymbol{r}^k$
    Solve $\mathbf{R}\boldsymbol{c} = \boldsymbol{b}$
    IQN step: $\boldsymbol{d}^{k+1}_{\hat{\Sigma}} = \tilde{\boldsymbol{d}}^k_{\hat{\Sigma}} + \mathbf{W}\boldsymbol{c}$
  end if
  $k = k + 1$
end while

applications considered. This is due to a very small dimension $k \times k$ of the triangular matrix $\mathbf{R}$ compared to the overall problem size and number of interface displacement degrees of freedom. The computational time spent for IQN-ILS acceleration is negligible compared to the other steps in the FSI scheme, in particular if the significant acceleration is factored in. However, both ϵ_{QR} and the number q of time steps from which data pairs are considered are problem-dependent in general, yet were found uncritical in all our numerical tests. If the relative computing time spent in the acceleration scheme were too high, an attractive alternative to the IQN-ILS scheme would be the modified interface quasi-Newton inverse multi-vector Jacobian method [34], which approximates the inverse Jacobian without any tuning parameters and whose cost scales linearly with the problem size.

4. Modelling aspects

This section is devoted to incorporating well-established mathematical models that handle typical challenges in computational biomechanics. This includes (i) outlet boundary conditions based on resistance and capacitance of cut-off regions, (ii) constructing suitable local coordinate systems to correctly incorporate anisotropic constitutive models and (iii) accounting for stressed reference geometries reconstructed from medical imaging. The extensions and improvements of the original SIDR scheme [52] presented in this section are novel, and our main contribution here is their inclusion in the semi-implicit PPE-based FSI scheme. The crucial aspect is to preserve the flexibility, generality, and robustness of the original scheme.

4.1. Windkessel outlets

When computational domains are truncated at one or multiple outlets, the influence of downstream flow on the solution is lost. Simple remedies for that prescribe, e.g., reference pressures or velocity profiles from volumetric flow data at the outlets, which can lead to stability issues depending on the flow regime. Yet, those quantities might not be readily available, being instead part of the sought solution itself. Windkessel models [70] are a valuable alternative, since they model the relation between pressure and outflow. Decomposing the Neumann boundary $\Gamma^t_{N,f}$ into non-overlapping outflow sections $\Gamma^t_{i,f}$, $i = 1, \ldots, N_{\mathrm{out}}$ (see, e.g., [2,51]), the mean pressure $p_{c,i}$ is advanced in time using

$$C_i \frac{\partial}{\partial t} p_{p,i} + \frac{p_{p,i} - p_{d,i}}{R_{d,i}} = Q_i(\boldsymbol{u}_f), \qquad p_{c,i} - p_{p,i} = R_{p,i}\, Q_i(\boldsymbol{u}_f), \quad i = 1, \ldots, N_{\mathrm{out}}$$

where C_i denotes the capacitance, $p_{p,i}$ and $p_{d,i}$ proximal and distal pressures, $R_{p,i}$ and $R_{d,i}$ proximal and distal resistances and $Q_i = \langle \boldsymbol{u}_f, \boldsymbol{n}_f \rangle_{\Gamma^t_{i,f}}$ is the outflow. Then, $p_{c,i}$ is weakly enforced via the traction condition

$$\boldsymbol{\sigma}_f \boldsymbol{n}_f = -p_{c,i}\, \boldsymbol{n}_f - \frac{\rho}{2} \boldsymbol{u}_f \left(\boldsymbol{u}_f \cdot \boldsymbol{n}_f \right)_- , \tag{48}$$

on $\Gamma^t_{i,f}$, $i = 1, \dots, N_{\text{out}}$, including backflow stabilisation (40) with $\alpha_b = 1$. A consistent time integration employing BDF-m schemes reads

$$C_i \sum_{j=0}^{m} \alpha_j^m p_{p,i}^{n+1-j} + \frac{p_{p,i}^{n+1} - p_{d,i}^{n+1}}{R_{d_i}} = Q_i(\boldsymbol{u}_f^{n+1}), \qquad p_{c,i}^{n+1} - p_{p,i}^{n+1} = R_{p,i}\, Q_i(\boldsymbol{u}_f^{n+1}), \quad i = 1, \dots, N_{\text{out}}.$$

However, $\boldsymbol{u}_f^{n+1}$ is not available for the Neumann condition enforcing $p_{c,i}^{n+1}$ via (48). To recover continuous pressure Dirichlet data on $\Gamma^t_{i,f}$, the L^2-projection (34) incorporates the extrapolated $\boldsymbol{u}_f^\star$, affecting the coupling scheme's performance. As shall be seen in Section 5, using higher-order extrapolation and BDF schemes is indeed possible, depending on the Robin and Windkessel parameters used. Choosing $Q_i(\boldsymbol{u}_f^{n+1}) \approx Q_i(\boldsymbol{u}_f^n)$ greatly improves temporal stability in the present scheme, as shall be seen in Section 5. Since the CFL condition introduces a time step limit, this approximation is perfectly reasonable taking the time scale of the cardiac cycle as reference.

4.2. Constructing the material orientation

For complex solid geometries, constructing a physiologically meaningful local material orientation to employ anisotropic material models is not straightforward. Examples in biomechanics are bifurcating, aneurysmatic or dissected vessels, the tracheobronchial tree or the heart (see, e.g., [3,9,71,72]). The computational algorithms operate based on a simple set of rules to achieve this task, while remaining fast, reliable and tunable by the user. Common approaches involve solving multiple auxiliary Laplace problems with user-specified boundary data, which, applied to a vessel network, might read

$$-\Delta \phi_l = 0 \qquad \text{in } \hat{\Omega}_s, \tag{49}$$

$$\phi_l = 0 \qquad \text{on } \hat{\Gamma}_{\text{in},s}, \tag{50}$$

$$\hat{\boldsymbol{n}}_s \cdot \nabla \phi_l = h_{l,i} \qquad \text{on } \hat{\Gamma}_{i,s},\ i = 1, \dots, N_{\text{out}}, \tag{51}$$

$$\hat{\boldsymbol{n}}_s \cdot \nabla \phi_l = 0 \qquad \text{on } \hat{\Sigma} \cup \hat{\Gamma}_{R,s}, \tag{52}$$

where the auxiliary scalar ϕ_l for the longitudinal orientation is prescribed at the inlet face of the solid $\hat{\Gamma}_{\text{in},s}$, normal fluxes $h_{l,i}$ are prescribed at the solid outlet faces $\hat{\Gamma}_{i,s}$, $i = 1, \dots, N_{\text{out}}$ and zero fluxes are enforced at the interface and exterior boundary. The $h_{l,i}$ are tuned to yield ϕ_l with a large enough gradient, such that

$$\boldsymbol{e}_2 := \frac{\nabla \phi_l}{\|\nabla \phi_l\|} \tag{53}$$

approximates the longitudinal direction $\boldsymbol{e}_2$ reasonably well. In a similar manner, a scalar ϕ_n to approximate the tissue-normal direction can be constructed via

$$-\Delta \phi_n = 0 \qquad \text{in } \hat{\Omega}_s, \tag{54}$$

$$\phi_n = 0 \qquad \text{on } \hat{\Sigma}, \tag{55}$$

$$\hat{\boldsymbol{n}}_s \cdot \nabla \phi_n = 0 \qquad \text{on } \hat{\Gamma}_{\text{in},s} \cup \hat{\Gamma}_{i,s},\ i = 1, \dots, N_{\text{out}} \tag{56}$$

$$\hat{\boldsymbol{n}}_s \cdot \nabla \phi_n = h_n \qquad \text{on } \hat{\Gamma}_{R,s}, \tag{57}$$

setting appropriate values h_n to achieve a reasonable tissue-normal direction $\boldsymbol{e}_3 := \nabla \phi_n / \|\nabla \phi_n\|$. This rule-based assignment of boundary conditions including tuning parameters is well suited for curved, bulging or bifurcating vessels, but not for changes that are limited to the cross section of the vessel alone. A typical example for such a configuration is encountered in aortic dissection, where the single original lumen splits into so-called true and false lumina (see Fig. 1 or, e.g., [73–75]). Then, this requires detection of the tissue layer separating these lumina and assignment of proper boundary conditions or even decomposition into several subproblems to obtain a proper material orientation in every part of the dissected vessel. As distinguishing different regions of the solid might,

Fig. 1. Finite element discretisation of a dissected aortic arch: adventitia (red), media (peach) and flap (light blue) regions of the tissue and lumen (grey). Complete mesh (left), cut aortic arch revealing lumen mesh (middle) and cut aortic arch showing tissue elements only (right). (For interpretation of the references to colour in this figure legend, the reader is referred to the web version of this article.)

however, increase the need for further tuning parameters or manually provided markers or reference points, such an approach is inappropriate for clinical application.

We overcome this by replacing the second step, resulting in a more flexible algorithm. The averaged normal vector on the fluid–structure interface is extrapolated into the structural domain to approximate the tissue normal direction, which is even applicable in parts that are in contact with fluid from both sides. In a first step, normal vectors $\hat{\boldsymbol{n}}_s$ on the fluid–structure interface $\hat{\Sigma}$ are determined for all elements lying on $\hat{\Sigma}$. Afterwards, the mean orientations of all elements touching the previously marked element layer are determined, taking each element's neighbours into account. This second step is repeated until the interface normal, later to be used as $\boldsymbol{e}_3$, is set in all elements. It is crucial to consider either only data from the first neighbour of each element that has an orientation, or – which is the alternative we employ – consider all neighbours of a given element, which have a radial direction $\boldsymbol{e}_{3,j}$ deviating from the first encountered neighbour with orientation $\boldsymbol{e}_{3,i}$, satisfying

$$\alpha_{\text{tol}} \geq \arccos\left(\frac{\boldsymbol{e}_{3,i} \cdot \boldsymbol{e}_{3,j}}{\|\boldsymbol{e}_{3,i}\| \, \|\boldsymbol{e}_{3,j}\|}\right). \tag{58}$$

This means that the normal direction $\boldsymbol{e}_{3,j}$ from neighbour j is only incorporated, if the angle between $\boldsymbol{e}_{3,j}$ and $\boldsymbol{e}_{3,i}$ from the first encountered neighbour deviate less than α_{tol}. Afterwards, a few number of conditional averaging cycles using condition (58) again suffice to obtain a satisfactory vector field. Note also that the tissue circumferential direction $\boldsymbol{e}_1$, constructed from the normal $\boldsymbol{e}_3$ and longitudinal directions $\boldsymbol{e}_2$, might be inverted. Consequently, this method is only applicable when the tissue's response does not change by inverting the circumferential direction $\boldsymbol{e}_1$, which is fortunately the case for symmetric fibre reinforcements typically used in the cardiovascular context.

The extrapolation of $\hat{\boldsymbol{n}}_s$ into $\hat{\Omega}_s$ is then directly used as the tissue-normal direction $\boldsymbol{e}_3$, while the step to generate the longitudinal orientation $\boldsymbol{e}_2$ remains unchanged (see, e.g., [3,72,76]). Based on the normalised longitudinal direction $\boldsymbol{e}_2$ and normal direction $\boldsymbol{e}_3$, the circumferential direction is defined as

$$\boldsymbol{e}_1 := \frac{\boldsymbol{e}_2 \times \boldsymbol{e}_3}{\|\boldsymbol{e}_2 \times \boldsymbol{e}_3\|}. \tag{59}$$

The mean fibre directions $\boldsymbol{m}_i$, symmetrically inclined by some angle α_c from circumferential to longitudinal direction, are then conveniently constructed via

$$\boldsymbol{m}_4 := \frac{\boldsymbol{e}_1 + \boldsymbol{e}_2 \tan(\alpha_c)}{\|\boldsymbol{e}_1 + \boldsymbol{e}_2 \tan(\alpha_c)\|}, \quad \boldsymbol{m}_6 := \frac{\boldsymbol{e}_1 + \boldsymbol{e}_2 \tan(-\alpha_c)}{\|\boldsymbol{e}_1 + \boldsymbol{e}_2 \tan(-\alpha_c)\|}. \tag{60}$$

These mean fibre directions $\boldsymbol{m}_i$, $i = 4, 6$ then compose the structural tensor $\boldsymbol{A}_i := \boldsymbol{m}_i \otimes \boldsymbol{m}_i$ and thereby enter the invariants $I_i := \boldsymbol{C} : \boldsymbol{A}_i$ contributing to the stress tensor $\boldsymbol{P}$ given in Eq. (9), see Section 2. The overall algorithm to

construct physiologically meaningful material orientation vectors $\boldsymbol{e}_1$ and $\boldsymbol{e}_2$ with extrapolated interface normal and conditional averaging is summarised in Algorithm 2.

Algorithm 2 Material orientation algorithm with conditional averaging

1: Solve the auxiliary Laplace problem (49)–(52) for ϕ_l.
2: Compute the longitudinal direction $\boldsymbol{e}_2$ via (53).
3: Set $\boldsymbol{e}_3 = \hat{\boldsymbol{n}}_s$ in all elements on $\hat{\Sigma}$.
4: **while** $\boldsymbol{e}_3$ not set in all elements **do**
5: On each element, find neighbours with $\boldsymbol{e}_3$ set and store $\boldsymbol{e}_{3,i}$ being the *first* encountered neighbour's $\boldsymbol{e}_3$.
6: Average all neighbour's orientations $\boldsymbol{e}_{3,j}$ for which (58) holds and assign the average $\boldsymbol{e}_3$.
7: **end while**
8: **while** Executed less than N_{avg} smoothing cycles **do**
9: Average $\boldsymbol{e}_{3,i}$ on each element, taking neighbour's directions $\boldsymbol{e}_{3,j}$ into account if (58) is met.
10: **end while**
11: Compute $\boldsymbol{e}_1$ given $\boldsymbol{e}_2$ and $\boldsymbol{e}_3$ via (59).

For vessels with a curved centreline, bifurcations or even aneurysms, material orientations based on two Laplace problems with suitable boundary conditions can yield satisfactory results as, e.g., shown in our previous work [52] for an idealised abdominal aortic aneurysm. As already pointed out, however, tissue layers wetted from both sides demand at least region-based assignment of boundary conditions. To highlight improvements achieved with Algorithm 2, a suitable orientation for a patient-specific aortic dissection geometry provided by Bäumler et al. [2] is constructed. Fig. 1 depicts the discretised aortic arch with adventitia (red), media (peach) and dissection flap (blue) tissue regions and the lumen (grey). We construct the longitudinal material orientation via Eqs. (49)–(53) using $h_{l,i} = 100$, resulting in the scalar field ϕ_l (Fig. 2, left) and vector field $\boldsymbol{e}_2$ (Fig. 2, right).

Solving another Laplace equation requires not only a subdivision into regions, but also detecting a specific side of the dissection flap. As spatial discretisations of such cases can lead to rather smooth transitions in the flap's surface mesh (see Fig. 1, right) more involved techniques or even manual intervention are necessary here. Thus, assigning appropriate boundary conditions is non-trivial, leading, e.g., for $h_n = 100$ in (57) to a scalar field ϕ_n as shown in Fig. 2 (middle). As depicted in Fig. 3, such an approach is indeed applicable for obtaining a material orientation in the media and adventitia layers (wetted from a single side only); however, in the flap region (wetted from both sides), the constructed $\boldsymbol{e}_1$ does not even remotely approximate the expected circumferential direction. A suitable orientation can be constructed by using Algorithm 2 with $\alpha_{\text{tol}} = 120°$ for conditional averaging and $N_{\text{avg}} = 5$ cycles of averaging after initial extrapolation of the interface normal. Inspecting the vector fields in Fig. 3, substantial improvements are obvious.

The proposed method improves versatility of the material orientation algorithm and drastically reduces tuning. The parameters $h_{l,i} = 100$, $\alpha_{\text{tol}} = 120°$ and N_{avg} yield great results for the presented aortic dissection case and all numerical examples considered in Section 5 (where the standard algorithm delivers good results as well). Due to the vast complexity of FSI modelling of aortic dissection, detailed, patient-specific simulations and investigations are postponed to future work, and the focus here is on demonstrating the orientation algorithm's applicability only.

4.3. Stressed reference geometries

In patient-specific haemodynamic simulations, or generally in scenarios where the structure is already loaded during imaging (to construct the computational domain), the solid stress state already present at the time of image acquisition – the prestress – is unknown, but might not be negligible. In the cardiovascular system, computed tomography and magnetic resonance images are taken during the diastolic phase under corresponding flow conditions. As a matter of fact, regardless of when in the cardiac cycle images are taken, the quiescent state would never be reached and a certain pressure level is maintained at any point. Therefore, this initial loading can have a large influence on the overall response, such that prestress effects cannot be neglected [2,56,77].

From a continuum mechanics point of view, several possibilities exist, the most popular ones being: (i) find a new stress-free reference geometry of the solid, from which a newly defined deformation field maps to the deformed configuration (see, e.g., [78]), or (ii) incorporate a prestress tensor $\boldsymbol{S}_0$ in the solid's balance of momentum,

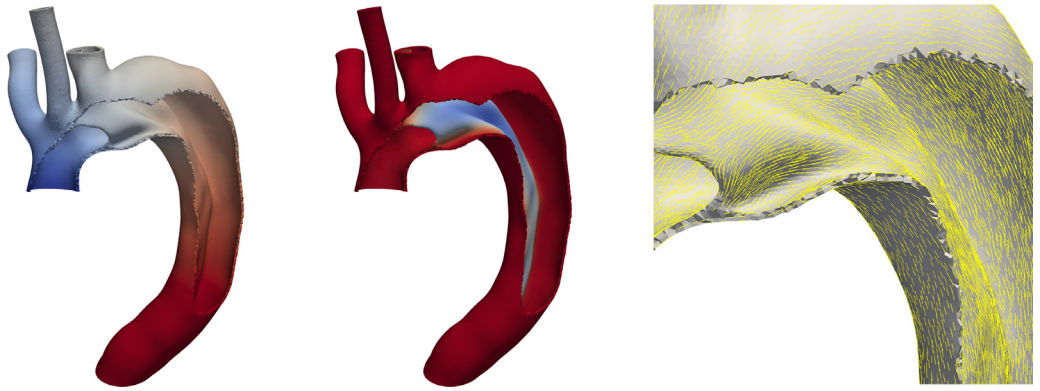

Fig. 2. Constructing the material orientation in the aortic arch region: solutions to the auxiliary Laplace problems ϕ_l (left) and ϕ_n (middle) with lower values in blue and higher values in red. Longitudinal directions $\boldsymbol{e}_2$ based on ϕ_l in dissection flap (right). (For interpretation of the references to colour in this figure legend, the reader is referred to the web version of this article.)

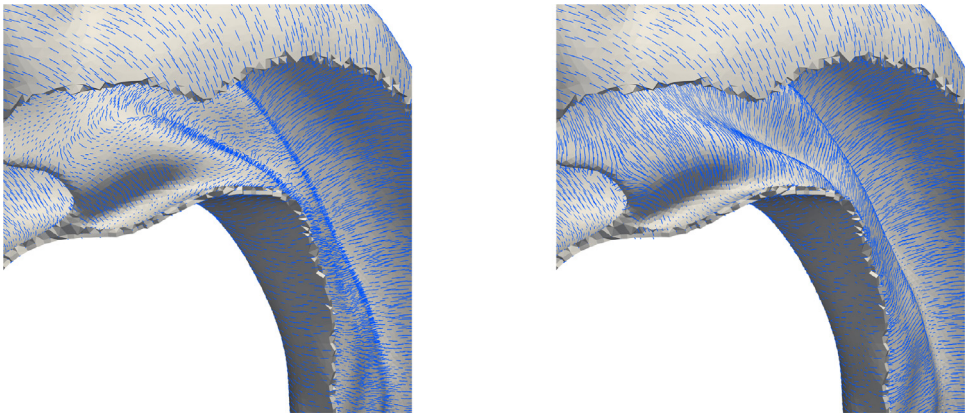

Fig. 3. Comparison of the circumferential direction $\boldsymbol{e}_1$ in the dissection flap: approach solving a second Laplace equation (left) and Algorithm 2 using an extrapolated interface normal (right). In the flap region, only the latter approach gives satisfactory results.

equating fluid tractions under diastolic flow conditions [56]. We herein employ (ii), since it can be straightforwardly incorporated into existing structural mechanics solvers. So, we replace Eq. (36) by its static counterpart including prestress to solve for a vector field $\boldsymbol{d}_0^{k+1}$. This displacement $\boldsymbol{d}_0^{k+1}$ enters the prestress tensor $\boldsymbol{S}_0$ using the same material law and the basic relation $\boldsymbol{P} = \boldsymbol{F}\boldsymbol{S}$ as [56]

$$\boldsymbol{P} = \boldsymbol{F}(\boldsymbol{d}_0^{k+1})\left[\boldsymbol{S}(\boldsymbol{d}_0^{k+1}) + \boldsymbol{S}_0(\boldsymbol{d}_0^{k})\right],$$

which results in static equilibrium including the prestress tensor $\boldsymbol{S}_0$:

$$-\nabla\cdot\left[\boldsymbol{P}(\boldsymbol{d}_0^{k+1}) + \boldsymbol{F}(\boldsymbol{d}_0^{k+1})\boldsymbol{S}_0(\boldsymbol{d}_0^{k})\right] = \boldsymbol{0} \quad \text{in} \quad \hat{\Omega}_s. \tag{61}$$

Starting from the quiescent state and ramping up the inlet conditions, flow quantities are kept fixed at a user-specified reference time t_0, which corresponds to the imaging data, and Eq. (61) is solved until the convergence criteria

$$\left\|\boldsymbol{d}_0^{k+1} - \boldsymbol{d}_0^{k}\right\|_{\max} < \epsilon_{\text{abs}}^{d_0} \quad \text{and} \quad \left\|\boldsymbol{d}_0^{k+1} - \boldsymbol{d}_0^{k}\right\| < \left\|\boldsymbol{d}_0^{k+1}\right\|\epsilon_{\text{rel}}^{d_0} \tag{62}$$

are fulfilled. Afterwards, we set $\boldsymbol{d}_0 = \boldsymbol{d}_0^{k+1}$ and keep $\boldsymbol{S}_0(\boldsymbol{d}_0)$ fixed. Then, we can directly apply the standard SIDR scheme, with the solid momentum equation incorporating $\boldsymbol{S}_0$:

$$\rho_s\frac{\partial^2}{\partial t^2}\boldsymbol{d}_s - \nabla\cdot\left[\boldsymbol{P}(\boldsymbol{d}_s) + \boldsymbol{F}(\boldsymbol{d}_s)\,\boldsymbol{S}_0(\boldsymbol{d}_0)\right] = \boldsymbol{0} \quad \text{in} \quad \hat{\Omega}_s. \tag{63}$$

To efficiently tackle Eq. (61), we combine adaptive, load-driven pseudo timestepping with Aitken relaxation and a continuation technique. That is, we actually solve Eq. (63) with $\eta_s^R = 0$, but since we only search for a stationary state, we are free to choose large physical mass- and stiffness-proportional damping and lower tolerance settings. Applying a continuation method, the diastolic fluid load is scaled from 0 to 1 via a parameter η_c, while the density ρ_s and viscous parameter c_e are successively lowered from initially increased values to ease convergence to the desired ones over N_c steps. Simultaneously, the sought $\boldsymbol{d}_0^{k+1}$ is updated using Aitken's relaxation (44) and the pseudo time step size is increased once less than N_{nl} Newton steps per nonlinear solve are needed. The pseudo time integration is stopped once a steady-state is reached, i.e.,

$$\left\| \ddot{\boldsymbol{d}}_s^{k+1} \right\| < \epsilon_{\text{rel}}^{\ddot{d}_0} \left\| \boldsymbol{d}_s^{k+1} \right\|, \tag{64}$$

and the convergence criteria (62) are fulfilled. For the convenience of the reader, the prestress procedure is summarised in Algorithm 3.

Algorithm 3 Incremental prestress algorithm

$n = 0$, $k = 0$, $l = 0$
Initialise $\boldsymbol{u}_f^n = \boldsymbol{0}$, $p_f^n = 0$
while $t < t_0$ **do**
    Update $\boldsymbol{u}_f^{n+1}$, p_f^{n+1} via fluid solver using $\boldsymbol{d}_s^{n+1} = \dot{\boldsymbol{d}}_s^{n+1} = \ddot{\boldsymbol{d}}_s^{n+1} = \boldsymbol{0}$
    $n = n + 1$
end while
Store time step data and set $\boldsymbol{u}_f^0 = \boldsymbol{u}_f^{n+1}$, $p_f^0 = p_f^{n+1}$
Initialise: $\boldsymbol{d}_0^k = \boldsymbol{d}_s^n = \dot{\boldsymbol{d}}_s^n = \ddot{\boldsymbol{d}}_s^n = \boldsymbol{0}$
while $l < N_c$ or (62) or (64) not fulfilled **do**
    Solve Eq. (63) with $\eta_s^R = 0$, $\eta_c \boldsymbol{\sigma}_f(\boldsymbol{u}_f^0, p_f^0)$ and $\boldsymbol{S}_0(\boldsymbol{d}_0^k)$ for $\boldsymbol{d}_0^{k+1}$
    Relaxed update: $\boldsymbol{d}_0^{k+1} = \omega_k \boldsymbol{d}_s^{n+1} + (1 - \omega_k)\boldsymbol{d}_0^k$
    $k = k + 1$
    if Nonlinear solver converged in less than N_{nl} steps **then**
        Increase pseudo time step size
        if $l < N_c$ **then**
            Continuation method: decrease ρ_s, c_e and increase η_c
            $l = l + 1$
        end if
    end if
    $n = n + 1$
end while
Start SIDR scheme with $\boldsymbol{d}_0 = \boldsymbol{d}_0^{k+1}$, $\boldsymbol{d}_s^n = \dot{\boldsymbol{d}}_s^n = \ddot{\boldsymbol{d}}_s^n = \boldsymbol{0}$ and available time step data for $\boldsymbol{u}_f$ and p_f.

Note that driving the flow with a ramped inlet condition from the quiescent state is often needed, especially when using Windkessel models. This is another purpose for the fluid stepping included in Algorithm 3. Also, the combination of pseudo timestepping, relaxation and continuation methods is merely a placeholder for more advanced techniques common in nonlinear solid mechanics.

5. Numerical experiments

The computational tests in this section demonstrate the applicability of our framework in settings relevant to haemodynamics and human phonation. Starting with fluid flow in a straight pipe, we focus first on the coupling algorithm's performance, comparing fully implicit and semi-implicit Dirichlet and Robin variants, and IQN-ILS and Aitken acceleration schemes. Then, we investigate blood flow through an iliac bifurcation, including realistic material parameters and flow data, with all of the modelling aspects discussed herein. Lastly, we present initial findings in a two-dimensional setup of human phonation with realistic problem parameters, resulting in the typical oscillatory response of the vocal folds. The implementation is based on the finite element toolkit `deal.II` [79], preconditioning each iterative linear solve with algebraic multigrid methods provided by Trilinos' ML package [80].

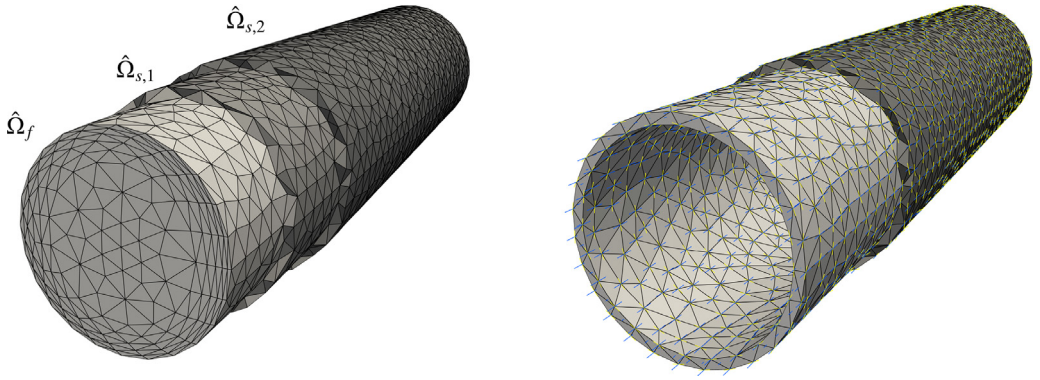

Fig. 4. Straight vessel geometry: fluid mesh with boundary layers and cut media $\Omega_{s,1}$ and adventitia $\Omega_{s,2}$ layers (left) and orientation vectors obtained via Algorithm 2, i.e., longitudinal (blue, $\hat{\boldsymbol{e}}_2$) and circumferential (yellow, $\hat{\boldsymbol{e}}_1$) orientation vectors (right). (For interpretation of the references to colour in this figure legend, the reader is referred to the web version of this article.)

5.1. Fluid flow in a straight pipe

Consider a straight cylindrical vessel of length $l = 5$ cm with a lumen radius $r_i = 0.5$ cm and two tissue layers with thickness $h_s = 0.05$ cm each, resolving media and adventitia tissue layers as depicted in Fig. 4. The material parameters are set in the physiologically relevant range, with $\rho_f = 1060$ kg/m^3 and $\rho_s = 1200$ kg/m^3 for fluid and solid densities, respectively. As this setup serves as a testing bed for several aspects introduced in Sections 3 and 4, we group our numerical experiments into subsections.

5.1.1. Pressure pulse

In a first series of computations, we investigate the coupling algorithm's performance and choose simpler constitutive models, which is admissible to some extent due to limited strains. The traction interface condition on the structure side, however, does consider large displacements. So, a linear-elastic solid with a Young's modulus of $E_s = 300$ kPa and Poisson's ratio of $\nu_s = 0.3$ is coupled to a Newtonian fluid with a dynamic viscosity of $\mu_f = 3.45$ mPa s. The vessel is fixed at both the inlet ($\hat{x}_1 = 0$) and the outlet ($\hat{x}_1 = l$), while zero tractions are weakly enforced at the fluid outlet boundary and the vessel's exterior surface ($c_e = 0$ and $k_e = 0$). The flow is driven by a prescribed traction $\boldsymbol{t}_f = (-p_{\text{in}}, 0, 0)^T$ at the inlet, defined via

$$p_{\text{in}}(t) = \begin{cases} \bar{p}_{\text{in}} \left[\frac{1}{2} - \cos(500\pi t)\right] & \text{for } t \leq 0.002, \\ \bar{p}_{\text{in}} & \text{for } 0.002 < t < 0.007, \\ \bar{p}_{\text{in}} \left[\frac{1}{2} + \cos(200\pi t)\right] & \text{for } 0.007 \leq t \leq 0.009, \\ 0 & \text{otherwise}, \end{cases} \tag{65}$$

smoothly ramping a pressure drop of $\bar{p}_{\text{in}} = 10$ mmHg ≈ 1333.22 Pa between inlet and outlet.

We employ a second-order temporal discretisation, i.e., linear extrapolation with BDF-2 and CH-α (ρ_∞=0) time integration using 30 uniform steps of size $\Delta t = 0.5$ ms. Neither GLS nor backflow stabilisation are employed, and convergence is solely based on the fluid pressure and structural displacement, setting $\epsilon^p_{\text{abs}} = 10^{-7}$ and $\epsilon^p_{\text{rel}} = 10^{-4}$ in Eq. (29) and $\epsilon^d_{\text{abs}} = 10^{-7}$ and $\epsilon^d_{\text{rel}} = 10^{-4}$ in Eq. (30). Irrespective of the coupling scheme, these criteria determine convergence, while we compare fully implicit and semi-implicit, Robin and pure Neumann interface conditions for the solid phase, or Aitken and IQN-ILS acceleration. For simplicity, we choose $\eta^R_s = 10\frac{\rho_f}{\Delta t}$ inspired by [29] and $\omega_0 = 10^{-2}$ as an initial relaxation in the first coupling step of Aitken's scheme and when there is no data available in the IQN-ILS acceleration. The IQN-ILS data matrices are built from vectors corresponding to the last $q = 5$ time steps, dropping columns based on $\epsilon_{QR} = 10^{-16}$.

Fig. 5 shows the accumulated coupling iterations over all 30 time steps, where one clearly observes faster convergence when using the IQN-ILS acceleration compared to standard Aitken relaxation. Semi-implicit variants of the FSI algorithm are not only faster in execution per coupling step, but also need fewer iterations to reach

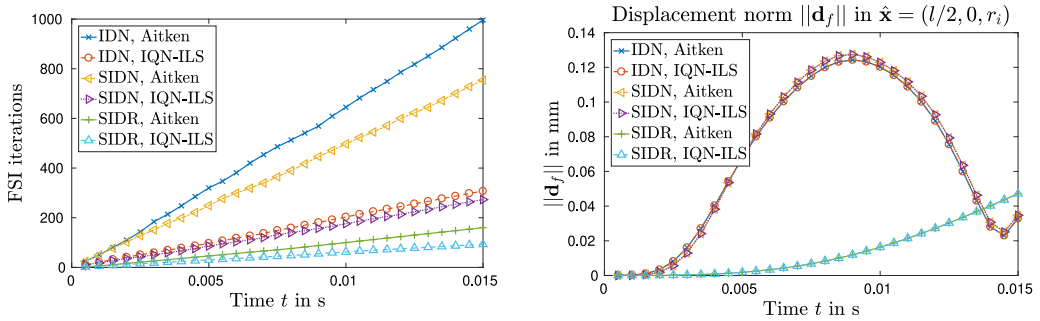

Fig. 5. Pressure pulse in a straight vessel: accumulated FSI coupling steps (left) and displacement in reference point (right). Semi-implicit Dirichlet–Neumann (SIDN) and Robin–Neumann (SIRN) variants and IQN-ILS acceleration outperform the classical implicit Dirichlet–Neumann (IDN) scheme and Aitken relaxation in terms of coupling iterations. Robin interface conditions accelerate convergence further, but the solution might change drastically with large η_s^R.

Table 3
Total FSI iterations and computing time for pressure pulse in a straight vessel: the semi-implicit Dirichlet–Neumann (SIDN) and Dirichlet–Robin (SIDR) schemes and IQN-ILS acceleration outperform the implicit Dirichlet–Neumann (IDN) scheme and Aitken relaxation.

	abs. FSI steps	rel. FSI steps	abs. time	rel. time
IDN, Aitken	971	10.67	$1.03{\cdot}10^3$ s	20.44
IDN, IQN-ILS	296	3.25	$3.06{\cdot}10^2$ s	6.07
SIDN, Aitken	730	8.02	$3.19{\cdot}10^2$ s	6.33
SIDN, IQN-ILS	262	2.89	$1.27{\cdot}10^2$ s	2.52
SIDR, Aitken	158	1.74	$7.46{\cdot}10^1$ s	1.48
SIDR, IQN-ILS	91	1.00	$5.04{\cdot}10^1$ s	1.00

convergence. For this specific example, this led to a substantial speed-up of over 20, as listed in Table 3. However, when comparing the semi-implicit Dirichlet–Neumann (SIDN) and semi-implicit Dirichlet–Robin (SIDR) variants, one needs to factor in changes in the obtained solution as well. Owing to a different weighting of the dynamic and kinematic coupling conditions dependent on the Robin parameter η_s^R, results may vary quite drastically. Taking the displacement norm of a reference point $\hat{\boldsymbol{x}} = (l/2, 0, r_i)$ as a reference, Fig. 5 clearly shows that (i) the acceleration scheme (Aitken or IQN-ILS) does not alter the solution itself when identical stopping criteria are used, (ii) the effect of semi-implicit coupling is almost insignificant in terms of the obtained solution, but (iii) the Robin interface condition may have a large impact on the solution itself. Thus, choosing a suitable η_s^R is a central aspect.

In the solid's momentum balance, the relevant integral stemming from the Robin interface condition is

$$\alpha_{\mathrm{f}}' \left\langle \boldsymbol{\varphi}, \eta_s^R \left(\boldsymbol{u}_f^\star - \dot{\boldsymbol{d}}_s^{n+1} \right) + J_f \boldsymbol{\sigma}_f \left(\boldsymbol{u}_f^\star, p_f^{k+1}, \mu_f^{n+1} \right) \boldsymbol{F}_f^{-T} \hat{\boldsymbol{n}}_s \right\rangle_{\hat{\Sigma}},$$

which transitions to a penalty-like term enforcing an explicit kinematic condition as $\eta_s^R \to \infty$. At the same time, a decreasing time step size Δt lowers the error in this very condition, since the extrapolation $\boldsymbol{u}_f^\star$ becomes more accurate. Introducing the Robin coefficient as $\eta_s^R = \alpha_R \frac{\rho_f}{\Delta t}$, one can transition from Robin to Neumann conditions by choosing α_R. As shown in Fig. 6, this has a rather predictable effect on the number of coupling steps, while the interface displacement may or may not follow an equally uniform relation. In this specific example, one observes rather surprising displacement responses right in the middle of the parameter sweep. Reducing the extrapolation order m_u of the fluid velocity mitigates this problem as numerical evidence indicates: In Fig. 7, the corresponding graph shows a much more expected transition to the solution obtained via the SIDN (SIDR with $\alpha_R = 0$) scheme. These tests suggest that the linearly extrapolated velocity of second-order improves accuracy but potentially impairs temporal stability, as indicated by increased FSI iteration counts in Fig. 7. Note here also that the mean pressure at the outlet is simply 0 and does not depend on the extrapolated velocity as would be the case when applying lumped parameter models.

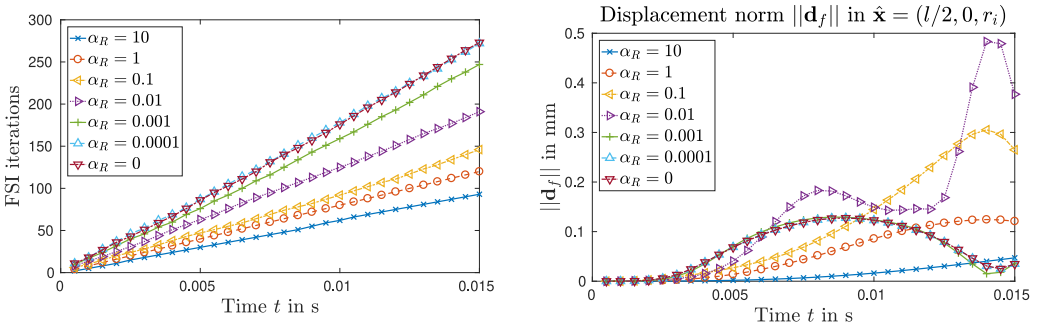

Fig. 6. Pressure pulse in a straight vessel: accumulated FSI coupling steps (left) and displacement in reference point (right) obtained via the SIDR scheme with scaled Robin parameter $\eta_s^R = \alpha_R \frac{\rho_f}{\Delta t}$ and second-order extrapolation ($m_u = 2$).

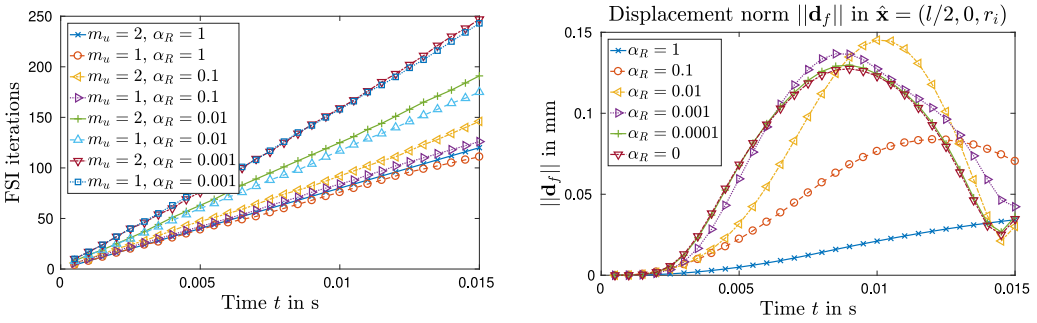

Fig. 7. Pressure pulse in a straight vessel: accumulated FSI coupling steps with fluid velocity extrapolation $m_u = 1$ or 2 (left) and displacement in reference point with $m_u = 1$ (right), obtained via the SIDR scheme with scaled Robin parameter $\eta_s^R = \alpha_R \frac{\rho_f}{\Delta t}$.

So, keeping the time step size fixed and decreasing the Robin parameter transitions to the SIDN scheme, where lower order velocity extrapolation improves stability. Similarly, lowering Δt and keeping η_s^R fixed cuts down the difference between SIDN and SIDR schemes. To showcase these relations, Table 4 lists the mean errors over all time steps taking the corresponding SIDN solution with identical time discretisation as reference. Second-order extrapolation of $\boldsymbol{u}_f^\star$, i.e., $m_u = 2$, is more likely to diverge with higher Robin parameters (since this shifts to explicit kinematic coupling), but minimises the discrepancy to the SIDN reference. For $m_u = 1$ the solution never diverges, and the difference to the reference diminishes as Δt decreases.

That being said, let us briefly comment on the Robin condition and the parameter choice. The choice $\eta_s^R = \alpha_R \frac{\rho_f}{\Delta t}$ (taken from [29]) is based on simplified model problems, where α_R is a suitably scaled maximum eigenvalue of the added-mass operator. In that sense, the α_R we choose in the tests might be rather high. On the other hand, our scheme shares the penalty-like term on the explicit kinematic coupling in the structure step in [41]. There, however, the coupling conditions are enforced via Nitsche's method with a parameter $\frac{10\mu_f}{h_e}$. Adopting the second interpretation and using the present parameters (in SI instead of CGS units), $\eta_s^R = 10000$, or $\alpha_R = 0.005$ in $\eta_s^R = \alpha_R \frac{\rho_f}{\Delta t}$, lie perfectly in the expected range.

Also, the solution obtained with the SIDN scheme is not fully converged in time for any Δt considered, but still serves as reference. A high Robin parameter with an extrapolation $\boldsymbol{u}_f^\star$ of order m_u is thus still of the same temporal order of accuracy, but the specific temporal error might be different. As the time step and element sizes go to zero, both the kinematic and dynamic interface conditions are fulfilled.

5.1.2. Pulsatile flow

In a second experiment, we restrict ourselves to the SIDR scheme with IQN-ILS acceleration but consider a more realistic setup. The main purpose is to qualitatively assess how the Robin scaling parameter influences both

Table 4
Average difference in displacements in $\hat{\boldsymbol{x}} = (l/2, 0, r_i)$ over all time steps between the SIDN reference and SIDR schemes with Robin parameter η_s^R. The second-order scheme ($m = m_u = 2$) is less robust than a variant using first-order extrapolation of $\boldsymbol{u}_f^\star$ ($m_u = 1$). With decreasing time step size, the difference between SIDN and SIDR diminishes.

m_u	η_s^R	$\Delta t = 0.125$ ms	$\Delta t = 0.25$ ms	$\Delta t = 0.5$ ms	$\Delta t = 1$ ms
2	2000	×	×	$5.77 \cdot 10^{-2}$	$6.04 \cdot 10^{-2}$
2	200	×	×	$1.05 \cdot 10^{-1}$	×
2	20	$5.42 \cdot 10^{-2}$	×	$9.80 \cdot 10^{-2}$	×
2	2	$7.36 \cdot 10^{-4}$	$2.40 \cdot 10^{-3}$	$7.58 \cdot 10^{-3}$	$1.76 \cdot 10^{-2}$
2	0.2	$7.08 \cdot 10^{-5}$	$2.13 \cdot 10^{-4}$	$4.98 \cdot 10^{-4}$	$1.76 \cdot 10^{-2}$
1	2000	$6.09 \cdot 10^{-2}$	$6.25 \cdot 10^{-2}$	$6.24 \cdot 10^{-2}$	$6.15 \cdot 10^{-2}$
1	200	$6.40 \cdot 10^{-2}$	$5.75 \cdot 10^{-2}$	$5.25 \cdot 10^{-2}$	$5.19 \cdot 10^{-2}$
1	20	$3.24 \cdot 10^{-2}$	$3.98 \cdot 10^{-2}$	$4.64 \cdot 10^{-2}$	$4.89 \cdot 10^{-2}$
1	2	$4.18 \cdot 10^{-3}$	$7.28 \cdot 10^{-3}$	$1.37 \cdot 10^{-2}$	$1.91 \cdot 10^{-2}$
1	0.2	$4.78 \cdot 10^{-4}$	$7.64 \cdot 10^{-4}$	$1.22 \cdot 10^{-3}$	$2.11 \cdot 10^{-3}$

performance and quantities of interest. So, we start by prescribing an inflow profile $\boldsymbol{u}_f = (u_1, 0, 0)^T$, with

$$u_1(r,t) = \bar{u}_{\text{in}(t)} \left(1 - \frac{r^2}{r_i^2}\right), \quad \bar{u}_{\text{in}(t)} = \eta_t(t)\left[4 + 6\sin^2(2\pi t + 0.1\pi)\right]$$

smoothly ramped in time from $t = 0$ to $T_r = 0.2$ s via

$$\eta_t(t) = \begin{cases} \sin^2\left(\frac{\pi t}{2T_r}\right) & \text{for } t \leq T_r, \\ 1 & \text{otherwise,} \end{cases} \tag{66}$$

to obtain a peak velocity of $u_{\max} \approx 0.5$ m/s (see Fig. 8). On the outflow boundary, the pressure level is determined according to a Windkessel model as described in Section 4.1, where $R_p = 1.5 \cdot 10^8$ Pa s/m^3, $R_d = 8 \cdot 10^8$ Pa s/m^3, $C = 1.5 \cdot 10^{-10}$ m^3/Pa and $p_p|_{t=0} = p_d = 0$ Pa are fixed, yielding a pressure fluctuation between ≈ 13 and 9 kPa, i.e., ≈ 97, 5 and 67.5 mmHg.

Now, we first aim to compare various constitutive models employed for both the solid and fluid phases. For the structure, we consider either linear elasticity (E), a St. Venant–Kirchhoff (SVK) model, neo-Hookean (NH) or Holzapfel–Gasser–Ogden (HGO) material, see Eqs. (9)–(12). In the first two cases, we use a Young's modulus $E_s = 400$ kPa and Poisson ratio $\nu_s = 0.3$, while in the latter two, a Poisson's ratio of $\nu_s = 0.499$ is selected to capture incompressible material behaviour. The tissue layers are assigned individual parameters, i.e., shear rates of $\mu_{s,1} = 62.1$ kPa and $\mu_{s,2} = 21.6$ kPa and fibre parameters $k_1 = 1.4$ kPa, $k_2 = 22.1$ and $\kappa_{c,1} = 0.12$, $\alpha_{c,1} = 27.47°$ or $\kappa_{c,2} = 0.25$, $\alpha_{c,2} = 52.88°$ following [72,81,82]. Viscoelastic tissue support with $k_e = 10^7$ N/m^3 and $c_e = 10^5$ Ns/m^3 is taken into account, which results in a displacement of $\approx$ 1mm, depending on the material model employed. In relative measures, this seemingly small displacement is already 20% of the vessel's radius and equals the tissue's thickness. For the fluid, we either employ a Newtonian model with $\mu_f = 3.45$ mPa s or alternatively a Carreau fluid ($\kappa_f = 1$, $a = 2$) with parameters $\eta_0 = 56$ mPa s, $\eta_\infty = 3.45$ mPa s, $\lambda_f = 3.313$ s and $\xi = 0.3568$ in (19) [83].

We keep the numerical settings as previously defined, i.e., choose the second-order time integration scheme with first-order accurate $m_u = 1$ to increase temporal stability. Additionally, GLS and backflow stabilisations are employed and a relative tolerance of 10^{-4} in the nonlinear structural solver is used. Three cardiac cycles of 0.5 s length are computed either with uniform timestepping or adaptive time step control enabled. Starting from $\Delta t^0 = 5 \cdot 10^{-4}$, the time step size may be chosen according to error estimates or predictor–corrector schemes available for BDF or Generalised-α time integration schemes, but herein we use

$$\Delta t^{n+1} = \max\left\{\Delta t_{\max}, 0.98\Delta t^n \min\left\{1.02, \frac{\text{CFL}_{\max}}{\max_e\{\text{CFL}_e\}}\right\}\right\}, \tag{67}$$

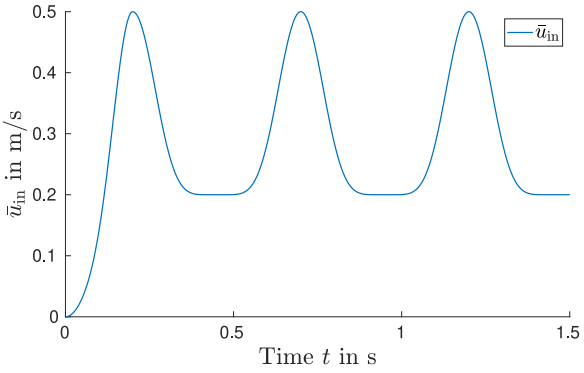

Fig. 8. Maximum prescribed inlet velocity $\bar{u}_{\text{in}}$ during three cycles from $t = 0$ to $t = 1.5$ s.

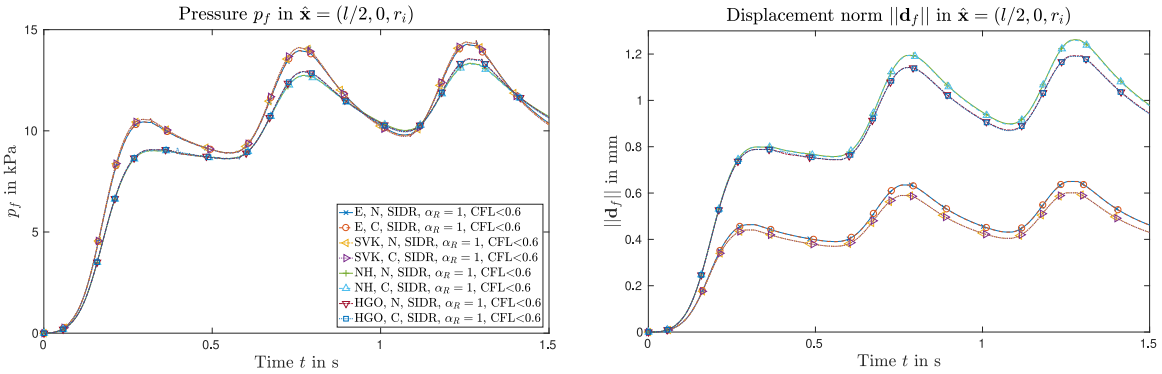

Fig. 9. Flow through a straight vessel: pressure (left) and displacement (right) in the reference point using the SIDR scheme with $\eta_s^R = \alpha_R \frac{\rho_f}{\Delta t^n}$ and adaptive timestepping ($\text{CFL}_{\max} = 0.6$). Comparison of linear elasticity (E), St. Venant–Kirchhoff (SVK), neo-Hookean (NH) and Holzapfel–Gasser–Ogden (HGO) solid models, combining them with Newtonian (N) or a Carreau (C) fluids.

to satisfy the Courant–Friedrichs–Lewy (CFL) condition by simply targeting a predefined maximum Courant number $\text{CFL}_{\max}$, based on the local one, CFL_e, defined on each element as

$$\text{CFL}_e = \max_i \left\{ \frac{\left| u_i - u_{m,i} \right| \Delta t^n}{h_i} \right\}, \quad i = 1, \dots, d\,, \tag{68}$$

with the directional element length h_i. Eq. (67) also includes additional "safety" measures, being a maximum growth factor of 1.02, a relaxation of 0.98 and a maximum time step size $\Delta t_{\max}$. Time steps leading to a maximum CFL number bigger than the specified target value are not repeated.

To compare the constitutive models in a simplified manner, only the solution in the reference point $\hat{\boldsymbol{x}} = (l/2, 0, r_i)$ on the fluid–structure interface is analysed by means of the structural displacement $\boldsymbol{d}_s$ and the fluid pressure p_f obtained applying the various models. In this more realistic setup leading to larger displacements and strains, differences are seen between displacement responses depending on the structural constitutive equation employed, as can be seen from Fig. 9. The observed quantities are not influenced by the fluid model, but the material parameters used for the different solids lead to significant changes. The fibre contributions in the HGO model render it stiffer, especially under large fibre strains and the linear elastic solid with its linear strain measure overestimates the displacement. The differences in expansion lead to an altered volumetric flow over the outlet boundary, such that the pressure wave is distinct as well.

Focusing on the overall number of executed coupling steps depicted in Fig. 10, we observe a negligible difference in the time steps and coupling iterations needed. As highlighted in Table 5, the mean number of FSI iterations per time step for all considered combinations is ≈ 2.2, which is on average enough to reduce the pressure and

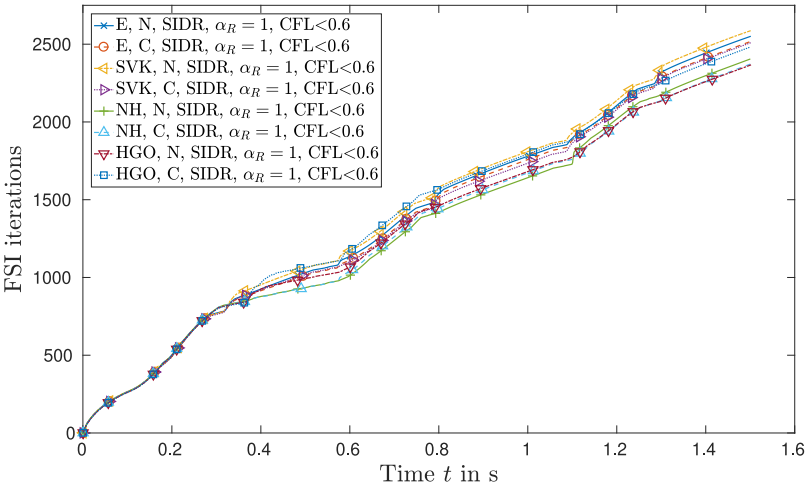

Fig. 10. Flow through a straight vessel: accumulated FSI iterations using the SIDR scheme with $\eta_s^R = \alpha_R \frac{\rho_f}{\Delta t^n}$ and adaptive timestepping ($\text{CFL}_{\text{max}} = 0.6$). Comparison of linear elasticity (E), St. Venant–Kirchhoff (SVK), neo-Hookean (NH) and Holzapfel–Gasser–Ogden (HGO) models, combining them with Newtonian (N) or Carreau (C) fluids.

Table 5
Flow through a straight vessel: comparison of SIDN and SIDR coupling schemes with uniform or adaptive timestepping ($\text{CFL}_{\text{max}} = 0.6$) in terms of time step number N_t, FSI coupling iterations N_{FSI} and mean FSI coupling steps per time step.

	E,N	E,C	SVK,N	SVK,C	NH,N	NH,C	HGO,N	HGO,C
N_t	1125	1122	1128	1124	1084	1085	1084	1085
N_{FSI}	2551	2517	2587	2510	2408	2372	2367	2482
N_{FSI}/N_t	2.27	2.24	2.29	2.23	2.22	2.19	2.18	2.29

displacement interface residuals by 10^4 owing to the combination of the SIDR scheme, IQN-ILS acceleration and a second-order accurate extrapolation of $\boldsymbol{d}_s$ and p_f used as initial guess.

Having seen the negligible impact of changing the constitutive models on the coupling scheme, let us now turn our attention to a detailed comparison of SIDN and SIDR schemes with $\eta_s^R = \alpha_R \frac{\rho_f}{\Delta t^n}$ using only St. Venant–Kirchhoff and Newtonian models to decrease the numerical effort. To diminish the influence of exterior viscoelastic support, we set $c_e = k_e = 0$ and consider the first-order scheme (BDF1 and trivial "extrapolation") to increase temporal stability.

As expected, the SIDR solution converges to the SIDN reference, as shown in Fig. 11 using a fixed $\eta_s^R = 20000$ and decreasing Δt. Zooming in on the third cycle's maximum displacement and pressure at $t = 1.26$ s, one also observes a decreasing phase shift as $\Delta t \to 0$ for the Robin variants, and that the pressure obtained via the SIDN scheme fluctuates around the assumed exact solution. These fluctuations are triggered by the added-mass effect being stronger as $\Delta t \to 0$, while the kinks in the pressure in the SIDR variants stem from backflow stabilisation being activated abruptly. Finally, comparing these results to those obtained with the SIDR scheme with adaptive stepping (see Fig. 12), we see that phase and amplitude match well even for $\alpha_R = 10$, which led to a severe phase lag and change in amplitude in the previous setup. Also, on the scale of one cycle, the oscillations in the SIDN pressure are no longer visible.

Naturally, the overall number of time steps and FSI coupling steps are vastly different, as Table 6 highlights: any of the presented parameter combinations needs approximately 3 FSI coupling iterations to reach convergence, and given equal effort spent per time step, the number of executed time steps dictates the overall time spent. Through this rationale, it is not surprising that the SIDR variant with adaptive stepping, which leads with $\text{CFL}_{\text{max}} = 0.6$ to 1880 time steps, is the fastest option. It is up to 26 times faster than the SIDN reference or 5 times faster than the SIDR run with a fixed time step size of $\Delta t = 2.5 \cdot 10^{-4}$, which lead to a comparable solution. That being said, let

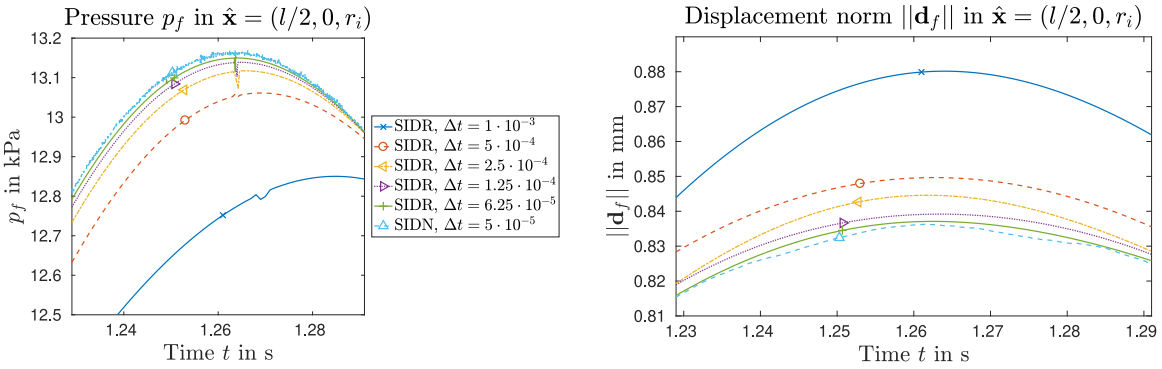

Fig. 11. Pulsatile flow through a straight pipe: zoom-in on pressure and displacement in a reference point to compare SIDR variants with $\eta_s^R = 20000$ to the SIDN scheme. The solutions converge as $\Delta t \to 0$ and the Robin variants feature no fluctuations caused by increased added-mass instabilities, only the abruptly activated backflow stabilisation leads to a visible kink in the pressure.

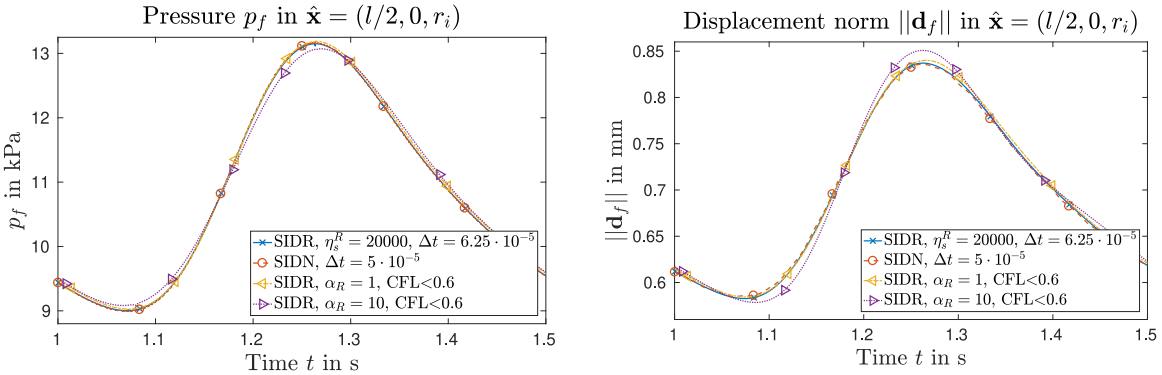

Fig. 12. Pulsatile flow through a straight pipe: last cycle from $t = 1$ to 1.5 s comparing pressure and displacement in the reference point obtained via SIDN and SIDR schemes. Adaptive timestepping with $\eta_s^R = \alpha_R \frac{\rho_f}{\Delta t^n}$ and $\text{CFL}_{\max} = 0.6$ matches phase and amplitude well.

Table 6
Pulsatile flow through a straight pipe: absolute (relative) time step number, FSI coupling iterations and computing time using SIDN and SIDR variants with fixed time step size or $\text{CFL}_{\max} = 0.6$. With adaptive time step control, sufficient accuracy is achieved in overall fewer steps, leading to a substantial speed-up.

	Time steps	FSI coupling steps	Time in 10^3 s
SIDN, $\Delta t = 1 \cdot 10^{-4}$ s	15000 (12.7)	45101 (12.8)	89.5 (12.8)
SIDN, $\Delta t = 5 \cdot 10^{-5}$ s	30000 (25.4)	91431 (26.0)	180.3 (25.8)
SIDR ($\eta_s^R = 20000$), $\Delta t = 1 \cdot 10^{-3}$ s	1500 (1.3)	4474 (1.3)	8.9 (1.3)
SIDR ($\eta_s^R = 20000$), $\Delta t = 5 \cdot 10^{-4}$ s	3000 (2.5)	8950 (2.5)	17.8 (2.5)
SIDR ($\eta_s^R = 20000$), $\Delta t = 2.5 \cdot 10^{-4}$ s	6000 (5.1)	17943 (5.0)	35.7 (5.1)
SIDR ($\eta_s^R = 20000$), $\Delta t = 1.25 \cdot 10^{-4}$ s	12000 (10.2)	35956 (10.2)	71.5 (10.2)
SIDR ($\eta_s^R = 20000$), $\Delta t = 6.25 \cdot 10^{-5}$ s	24000 (20.3)	72150 (20.5)	143.2 (20.5)
SIDR ($\alpha_R = 1$), $\text{CFL}_{\max} = 0.6$	1180 (1.0)	3516 (1.0)	7.0 (1.0)
SIDR ($\alpha_R = 10$), $\text{CFL}_{\max} = 0.6$	1184 (1.0)	3517 (1.0)	7.0 (1.0)

us remark that such concrete numbers, comparisons and gains in computational performance are of course heavily problem-dependent, but can be expected up to some degree, when a periodic inflow such as the present one are considered.

Before moving on to a more complex example, let us summarise the results of these first numerical experiments:

- Semi-implicit variants iteratively coupling only the fluid's pressure and structural displacement yield good results when compared to the fully implicit reference solutions when the time step size is chosen small enough, fulfilling a standard CFL-condition.
- Using Robin interface conditions on the structure side can greatly reduce the iteration counts, but may alter the solution when the Robin parameter is too large. However, even when a large scaling parameter α_R is selected, decreasing the time step size (or maximum allowed CFL number, maximum error measure in an estimator or equivalent) and keeping the overall Robin parameter $\eta_s^R = \alpha_R \frac{\rho_f}{\Delta t^n}$ unchanged, the solution converges to the reference Dirichlet–Neumann solution.
- An outlet pressure obtained from combining a Windkessel model with adaptive timestepping in a pulsatile flow setting was only found stable when using a first-order velocity extrapolation, hinting at the expected difference in stability properties for first- and second-order time integration and extrapolation schemes. For practical applications, the SIDR variant proved to be a viable alternative, converging faster than the SIDN counterpart and yielding virtually identical results given a reasonable time step size.

5.2. Iliac bifurcation

In a second example in haemodynamics, we consider blood flow through an iliac bifurcation driven by physiological flow data. Here, all techniques and modelling aspects described in Sections 3 and 4 are taken into account, i.e., we use GLS, backflow stabilisation and an IQN-ILS-accelerated SIDR scheme, account for Windkessel outlets, an inflow profile remap, a stressed reference geometry, and construct a meaningful material orientation based on the interface normal.

An interface representation reconstructed from computed tomography images [84–86] is uniformly extended in outward normal direction by 1 mm, sweeping the volume representing the solid layer enclosing the lumen. The considered computational domain has a length of $\approx$ 11 cm and the mean inlet radius is $r_M \approx 7.1$ mm, while the outlets have mean radii of $\approx$ 7.8 and 8.6 mm. The discrete mesh is composed of $\approx 585 \cdot 10^3$ tetrahedra with $\approx 108 \cdot 10^3$ nodes, resulting in $\approx 1.19 \cdot 10^6$ overall degrees of freedom (using linear shape functions for $\boldsymbol{d}_s$, $\boldsymbol{u}_f$, $\boldsymbol{d}_f$, p_f and the projection variable ψ), as shown in Fig. 13. Also, we highlight the reference point on the fluid–structure interface, for which we will report results. Circumferential ($\boldsymbol{e}_1$) and longitudinal ($\boldsymbol{e}_2$) material orientations are approximated as laid out in Section 4.2, which results for this geometry in the vectors shown in Fig. 13 when using $\alpha_{\text{tol}} = 120°$, $N_{\text{avg}} = 5$ and $h_{l,i} = 100$, $i = 1, 2$ in Algorithm 2.

Regarding material parameters, we consider physiological values obtained from literature, that is, densities of $\rho_f = 1060$ kg/m^3 and $\rho_s = 1200$ kg/m^3, employ a Carreau fluid ($\kappa_f = 1$, $a = 2$) with parameters $\eta_0 = 56$ mPa s, $\eta_\infty = 3.45$ mPa s, $\lambda_f = 3.313$ s and $\xi = 0.3568$ in (19), taken from [83]. For the tissue, we employ the quasi-incompressible HGO model [57], i.e., Eq. (9), with parameters taken from [81,82] for medial tissue, neglecting other layers of the abdominal aorta. Further, we set $\nu_s = 0.499$ for the Poisson's ratio and $\mu_s = 62.1$ kPa for the shear rate, leading to a bulk modulus (for homogeneous isotropic linear elastic materials) of $\kappa_b = 2\mu_s(1+\nu_s)/(3-6\nu_s) \approx 3.1$ MPa. Fibre parameters are selected with $k_1 = 1.4$ kPa, $k_2 = 22.1$ and $\kappa_c = 0.12$, symmetrically inclining the mean fibre direction by $\alpha_c = 27.47°$ in Eq. (60) relative to the circumferential direction.

Concerning boundary conditions, the solid layer is completely fixed at the in- and outlet boundaries and surrounding tissue is accounted for using $k_e = 10^7$ N/m^3 and $c_e = 10^5$ Ns/m^3 in Eq. (7). A parabolic inflow profile is remapped onto the (slightly) non-circular profile using the technique introduced in [55], matching measured volumetric flow rates taken from [87]. Over the first $T_r = 0.5$ s, the inflow is ramped according to Eq. (66), starting from the quiescent state. Additionally, Windkessel parameters of $C_i = 1.5 \cdot 10^{-8}$ m^{4}s^2/kg, $R_{p,i} = 2 \cdot 10^8$ kg/m^{4}s, $R_{d,i} = 10^9$ kg/m^{4}s, $p_{d,i} = 7$ kPa and $p_{p,i}|_{t=0} = 0$ for $i = 1, 2$ are selected to obtain pressures in the physiological range [87]. Doing so, the fluid pressure in the reference point and the reference pressure $\bar{p}_f$ match well after the prestress phase is completed, as can be seen in Fig. 14, where the maximum inlet velocity $\bar{\boldsymbol{u}}_{\text{in}}$ is depicted as well. The remaining discrepancy is accepted, since further tuning the Windkessel parameters lies beyond the scope of this work.

To account for prestress, we perform a flow simulation until $t_0 = 2.5$ s, where a periodic solution of the isolated flow problem is already reached, but the pressure is on purpose not considered at its diastolic minimum. At this point, the traction exerted by the fluid onto the tissue is kept fixed, as detailed in Algorithm 3 . The pseudo timestepping is started with $\Delta t^0 = 1$ ms and the continuation method equally scales ρ_s, c_e and η_c over 50 increments. An

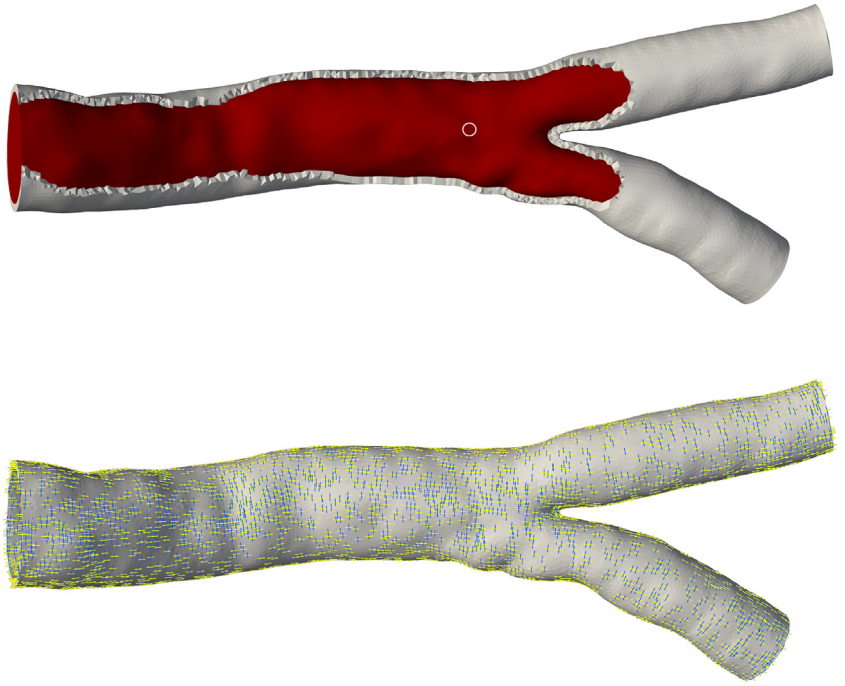

Fig. 13. Iliac bifurcation: structural finite element mesh (grey), revealing fluid mesh (red) and reference point on the fluid–structure interface (top) and circumferential ($\boldsymbol{e}_1$, blue) and longitudinal ($\boldsymbol{e}_2$, yellow) orientation vectors in the tissue layer (bottom). (For interpretation of the references to colour in this figure legend, the reader is referred to the web version of this article.)

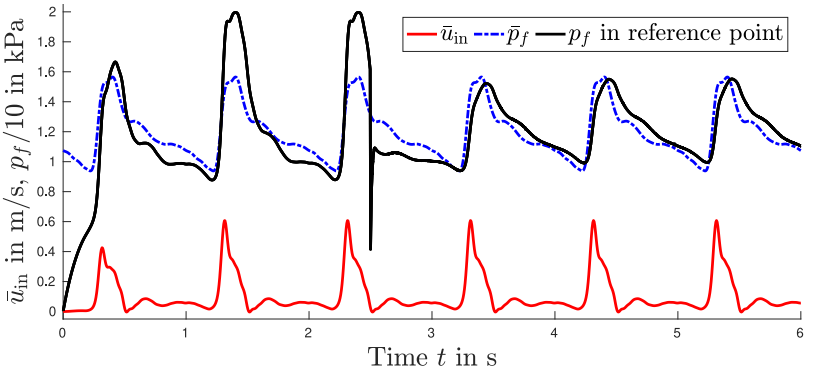

Fig. 14. Physiological maximum inlet velocity $\bar{\boldsymbol{u}}_{\text{in}}$, reference pressure $\bar{p}_f$ taken from literature [87] and computed pressure p_f in the reference point (see Fig. 13).

increase of 5% in the pseudo time step size up to $\Delta t_{\max} = 5$ ms and a load step increment is performed if less than $N_c = 3$ Newton steps are needed in the solid solve to reach convergence, while the initial relaxation parameter in Aitken's relaxation is $\omega_0 = 0.1$. Then, a quasi-static solution is obtained 83 pseudo time steps after applying the full load, using tight tolerances of $\epsilon_{\text{rel}}^{d_0} = 10^{-10}$ (and $\epsilon_{\text{abs}}^{d_0} = 10^{-20}$) in (62) and $\epsilon_{\text{rel}}^{\ddot{d}_0} = 10^{-3}$ in (64). As expected, the displacement field $\boldsymbol{d}_0$ resembles "inflating" the geometry by applying a pressure, as seen in Fig. 15. We want to stress again, however, that $\boldsymbol{d}_0$ is *not* to be understood as an initial displacement field when starting the FSI simulation, but captures the prestress $\boldsymbol{S}_0$ present in $\hat{\Omega}_s$ counteracting the fluid loads acting on the interface. In this sense, Fig. 15 does not show the initial condition for $\boldsymbol{d}_s$, but rather indicates which field $\boldsymbol{d}_0$ results in $\boldsymbol{S}_0$ to solve Eq. (61). The vector field $\boldsymbol{d}_0$ enters in the structure's momentum balance equation as given in Eq. (63), while

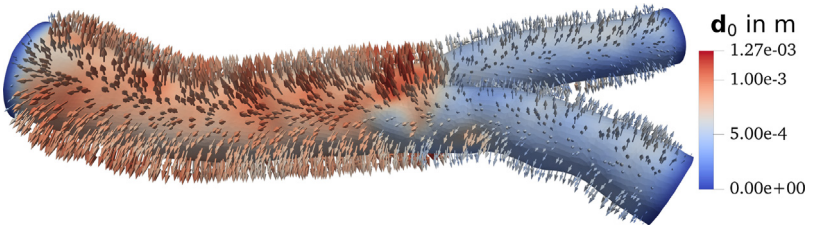

Fig. 15. Displacement field $\boldsymbol{d}_0$ obtained via Algorithm 3 with fluid forces generated at $t_0 = 2.5$ s.

Fig. 16. Blood flow in an iliac bifurcation: fluid velocity vectors in the cut vessel geometry. Maximal inlet velocity at $t = 5.31$ s (top) and largest displacement and pressure at 5.49 s (bottom). The rapid decrease in the inflow velocity causes a flow redirection.

the initial conditions of the structure's material displacement and velocity are zero, $\boldsymbol{d}_s^0 = \dot{\boldsymbol{d}}_s^0 = \mathbf{0}$ (see line 22 in Algorithm 3).

The pressure in the reference point shown in Fig. 14 exhibits large fluctuations as soon as we allow for displacement of the tissue. This indicates good stability properties of the prestress algorithm even if t_0 is not set at the end of the diastolic phase, i.e., if the preceding phase does not feature nearly steady inflow. Exemplarily, we present snapshots of the solution at $t = 5.31$ and 5.49 s in Fig. 16, where the inlet velocity is maximal at the former instant and displacement and pressure are maximal at the latter. Strong recirculations causing a deviation of the flow from the vessel centre axis result from decreasing the inflow rapidly and lead to large variations in viscosity. Further studying the specifics of the present solution might be of interest, but lies outside of this paper's scope and is hence postponed to future investigations. Instead, let us focus on the numerical performance of the scheme.

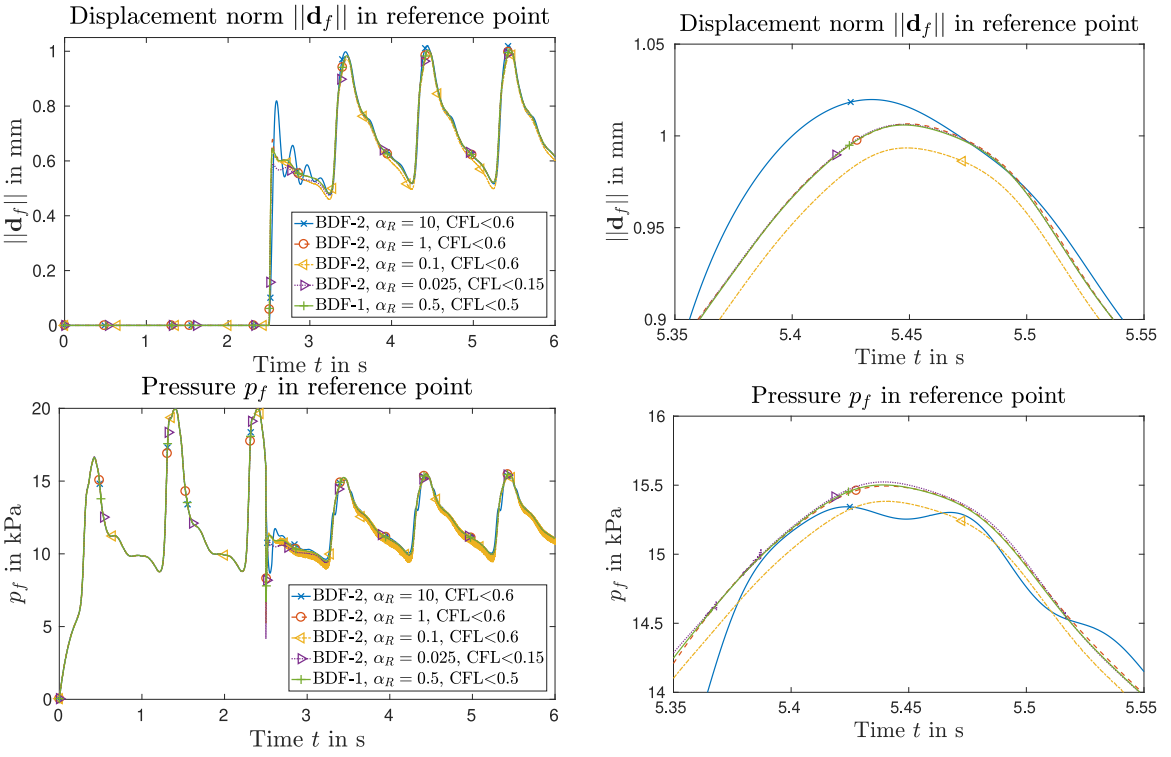

Fig. 17. Blood flow through an iliac bifurcation: structural displacement norm $\|\boldsymbol{d}_s\|$ (top) and fluid pressure p_f (bottom) in the reference point at the fluid–structure interface, overall view (left) and zoom-in on $t = 5.35$ to 5.55 s (right).

Similar to the first numerical tests, the fully second-order scheme was found to be too unstable, but can be improved substantially by using a first-order extrapolation of the fluid velocity (and using second-order accurate time integration and extrapolation schemes for all other quantities). Again, this effect is much less relevant for constant Δt or when replacing the Windkessel outlets by static traction boundaries. Starting from $\Delta t^0 = 1$ ms initially, we adapt the time step size based on CFL_e as defined in Eq. (68), additionally ensure $\Delta t \leq 5$ ms and allow for a maximum growth of 5% per time step. Setting different scaling parameters α_R in $\eta_s^R = \alpha_R \frac{\rho_f}{\Delta t^n}$, the solutions in the reference point converge, as depicted in Fig. 17. Initially, set $\mathrm{CFL}_{\max} = 0.6$ and compute two solutions with $\alpha_R = 10$ and $\alpha_R = 1$. A good match concerning amplitude and phase of pressure and displacement curves is already obtained, but further reducing the Robin parameter once again by a factor of 10 by setting $\alpha_R = 0.1$ leads to oscillations in the pressure. However, we can obtain a stable solution with $\mathrm{CFL}_{\max} = 0.15$ and $\alpha_R = 0.025$, which has an identical α_R to $\mathrm{CFL}_{\max}$ ratio, i.e., similar $\eta_s^R = \eta_s^R(\alpha_R, \mathrm{CFL}_{\max})$, but a smaller mean time step size. That being said, it is also worth noting that the SIDN scheme ($\alpha_R = 0$) is found unstable for this specific combination of adaptive timestepping and Windkessel parameters.

For comparison, Fig. 17 also contains results from a fully first-order scheme, which compares well to the BDF-2 variant. Strictly speaking, the latter is also first-order accurate in time due to the velocity extrapolation $\boldsymbol{u}_f^\star = \boldsymbol{u}_f^n$ ($m_u = 1$), which is needed for stability.

Turning our attention to the coupling algorithm's performance, one observes an increase in Pressure Poisson solves per time step at $t_0 = 2.5$ s due to FSI being "switched on" as can be seen in Fig. 18. Afterwards, the mean number of coupling steps per cardiac cycle stays almost constant, whereas before $t_0 = 2.5$ s, it simply indicates the number of accumulated time steps.

Depending on the targeted CFL number and resulting Δt, the number of accumulated PPE solves grows. With decreasing time step size, the actually selected Δt^{n+1} via Eq. (67) fluctuates, which suggests that further tuning of the safety parameters in Eq. (67) might be beneficial. However, decreasing the time step size simultaneously

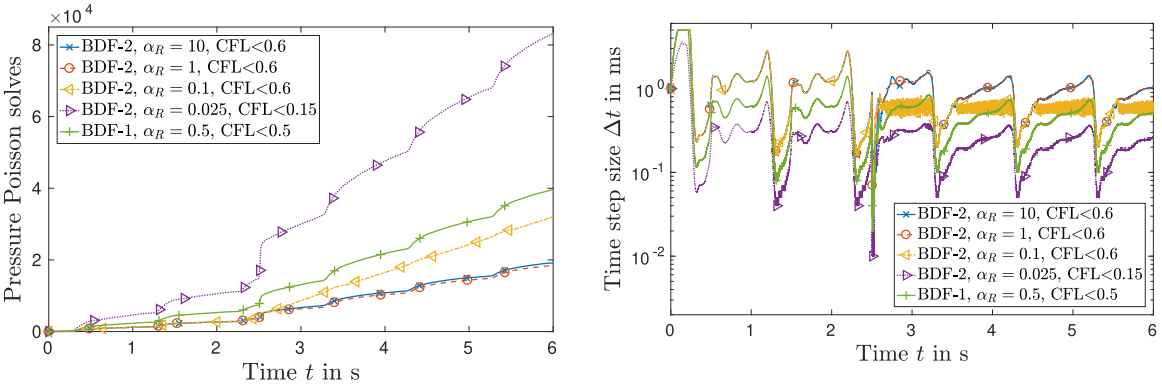

Fig. 18. Blood flow through an iliac bifurcation: accumulated pressure Poisson solves (left) and time step size (right). At $t_0 = 2.5$ s the prestress is calculated based on a pure flow simulation, after which the fluid–structure coupling is accounted for.

Table 7
Blood flow through an iliac bifurcation: Absolute (relative) time step number and coupling iterations in the FSI phase with various target CFL numbers and Robin scaling parameters α_R.

	Time steps	FSI steps	FSI-/time step
BDF-2, $\alpha_R = 10$, $\text{CFL}_{\max} = 0.6$	5445 (1.02)	15442 (1.05)	2.84 (1.03)
BDF-2, $\alpha_R = 1$, $\text{CFL}_{\max} = 0.6$	5356 (1.00)	14679 (1.00)	2.74 (1.00)
BDF-2, $\alpha_R = 0.1$, $\text{CFL}_{\max} = 0.6$	6985 (1.30)	28290 (1.93)	4.05 (1.48)
BDF-2, $\alpha_R = 0.025$, $\text{CFL}_{\max} = 0.15$	22143 (4.13)	68469 (4.66)	3.09 (1.13)
BDF-1, $\alpha_R = 0.5$, $\text{CFL}_{\max} = 0.5$	10703 (2.00)	32206 (2.19)	3.00 (1.10)

increases the added-mass effect, which together with a worsened initial guess due to fluctuations comprises two more reasons for an increased iteration count per time step as $\Delta t \to 0$.

As seen from Table 7, these effects show an increase in the mean coupling iteration count per time step, rendering the setup with $\text{CFL}_{\max} = 0.6$ the fastest. The solution with smaller Robin parameter turns out to be both the fastest and is almost identical to the reference solution with smallest α_R and CFL number. Changing the tolerances in the involved linear solvers, Newton method or coupling scheme, desired CFL or physical problem parameters might influence the numbers obtained here, but a large potential for possible gains in efficiency is evident.

5.3. Human phonation

We finally target human phonation, that is, the creation of voice by the vocal folds (VFs) interacting with air from the lungs (see, e.g., [4–7,88]). The main motivation for considering this demanding problem here are the considerable differences in physical parameters and flow regime. It also showcases the applicability of the semi-implicit scheme and IQN-ILS acceleration in a challenging context with high Reynolds number and low, but non-negligible added-mass effect. The geometry is slightly adapted from [88], and physiological parameters are taken from [5,88]. The symmetry plane of the glottis is considered as a channel from $x_1 = 0$ to $x_1 = L \approx 65.4$ mm and a height of $H = 18$ mm. The VFs and the 7.5 mm downstream positioned false VFs of 8.9 mm and 6.5 mm height are elastic. The resulting initial gap between the two VFs is 0.2 mm, as shown in Fig. 19. In doing so, we model glottal insufficiency where the two VFs do not come into contact during the oscillation cycle [89].

The Newtonian fluid representing air has a viscosity of $\mu_f = 0.019$ mPa s and a density of $\rho_f = 1.145$ kg/m^3 and is coupled with a linear elastic solid with a density of $\rho_s = 1200$ kg/m^3, a Young's modulus of $E_s = 20$ kPa and a Poisson's ratio of $\nu_s = 0.45$. Starting from the quiescent state, i.e., $\boldsymbol{u}_f = \boldsymbol{0}$, a quadratic inlet velocity profile at the left boundary at $x_1 = 0$ is smoothly ramped over the first $T_r = 0.01$ s via η_t, leading to

$$\boldsymbol{u}_f = (\eta_t 0.6, 0)^T, \quad \text{with} \quad \eta_t = \begin{cases} \sin^2\left(\frac{\pi t}{2T_r}\right) & \text{for } t \leq T_r, \\ 1 & \text{otherwise,} \end{cases}$$

Fig. 19. Human phonation example: computational domain considered (left) and close-up of the mesh on the top VFs' trailing edge (right) with points A ($\times$) and B ($\circ$) highlighted.

such that a constant maximum inlet velocity of 0.6 m/s is reached at $t = T_r$. This is different from many works found in literature that consider only fluid dynamics. The absence of self-excited motion requires imposing a fluctuating inlet velocity or pressure, but when FSI is accounted for, prescribing a fixed flow rate allows recovering the natural frequency of the VFs' oscillatory response [5–7]. A zero traction condition at the outlet at $x_1 = L$ enforces a zero reference pressure, while no-slip boundary conditions at the channel's walls are considered. The fluid domain and the linear elastic solid are both fixed at the channel's walls, such that the structure deforms due to the air flow, causing it to vibrate given the current set of parameters.

These boundary conditions lead to a maximum interglottal velocity of 35 m/s with a corresponding Reynolds number of $\mathrm{Re} = \mathcal{O}(1000)$ such that the mesh as depicted in Fig. 19 results in an element Reynolds number $\mathrm{Re}_e \approx 250$, which is defined similarly to the element CFL number (68),

$$\mathrm{Re}_e = \max_i \left\{ \frac{\rho_f |u_i - u_{m,i}| h_i}{\mu_f} \right\}, \quad i = 1, \dots, d, \tag{69}$$

where h_i is again the element length in direction $i = 1, \dots, d$. Judging from the element Reynolds number, the spatial grid is rather coarse and merely capable of resolving the main features. On the other hand, $\mathrm{CFL}_{\max} < 1$ requires a small time step size $\Delta t < 3.4 \times 10^{-6}$. In our numerical tests, $\mathrm{CFL}_{\max} = 0.2$ is set to remain shy of the stability limit, which is just an estimate to begin with. Therefore, a time interval from $t = 0$ to $T = 0.15$ s results in more than 4×10^5 time steps, which is why two space dimensions are considered within this work. A wider glottal channel – as often considered in literature – would decrease the intraglottal velocity and ease numerical treatment, weakening the high velocity gradients in the computational results. However, this numerical test is designed to showcase applicability of the solution algorithm in a challenging application in biomechanics outside of the haemodynamic regime.

Concerning the discretisation, we employ a first-order scheme, i.e., linearise with the last time step's solution combined with BDF-1 and CH-α ($\rho_\infty = 0$) time integration starting from $\Delta t^0 = 10^{-4}$ s with $\mathrm{CFL}_{\max} = 0.2$ in Eq. (67). Both GLS and backflow stabilisation are employed, and convergence is solely based on the fluid pressure and structure displacement, setting $\epsilon^p_{\mathrm{abs}} = 10^{-7}$ and $\epsilon^p_{\mathrm{rel}} = 10^{-3}$ in Eq. (29) and $\epsilon^d_{\mathrm{abs}} = 10^{-7}$ and $\epsilon^d_{\mathrm{rel}} = 10^{-3}$ in Eq. (30). The SIDR scheme with Robin parameter $\eta^R_s = \alpha_R \frac{\rho_f}{\Delta t^n}$ and IQN-ILS acceleration with unaltered settings, i.e., $\omega_0 = 10^{-2}$, $q = 5$ and $\epsilon_{QR} = 10^{-16}$ is considered.

After an initialisation phase, a periodic state is reached as indicated by the snapshots in Fig. 20: the pressure builds up due to the constrained flow through the glottal channel, causing the VFs to deform and consequently lowering the pressure, which in turn causes the elastic VFs to swing back into their original position and further due to inertia. Then, the cycle repeats, as the channel is narrowed again and onset pressure increases, such that the VFs oscillate in a periodic motion around their initial state.

This periodic motion, however, is constituted by multiple modes as analysed, e.g., in [6]. The deformation of the VFs is also not symmetric past a certain time, since (i) vortex shedding is induced and non-symmetric vortices form past the VFs given the high Reynolds number and (ii) glottal insufficiency (no contact between the two VFs) results in non-symmetric oscillations due to the lack of energy exchange between the VFs. Thus, the VFs' apex points A and B highlighted in Fig. 19 undergo a complex motion, of which the last four periods from $t \approx 0.12$–0.15 s are depicted in Fig. 21. A fundamental frequency of ≈ 130–150 Hz is observed, which lies perfectly in the expected range [4,88].

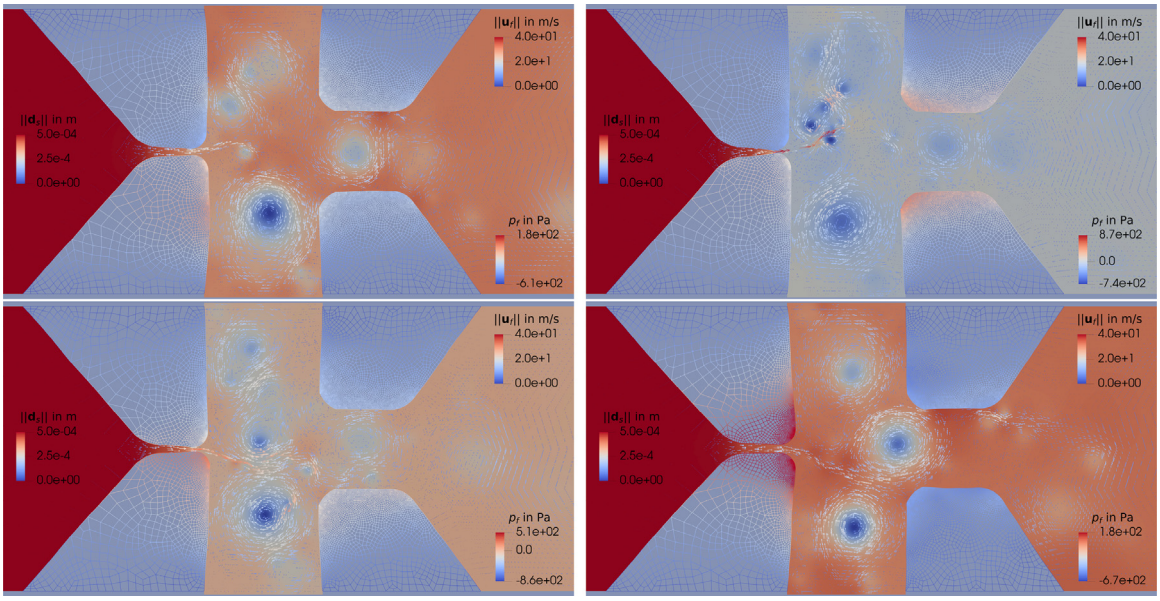

Fig. 20. Human phonation example: selected velocity vectors $\boldsymbol{u}_f$ over pressure p_f in the fluid and deformed solid mesh edges coloured by $\|\boldsymbol{d}_s\|$ at four distinct points in the self-excited, periodic motion of the VFs. The VFs return to their initial configuration (0.2 mm gap) from the previous oscillation (top left) and almost touch due to inertia (top right), which causes a strong jet triggering vortices past the VFs. This narrowing of the glottal channel causes the pressure to rise, deforming the VFs and opening up the channel again (bottom left). As the channel opens, the VFs deform maximally and the pressure gradient is lowered, after which the VFs return to their initial position to repeat this cycle.

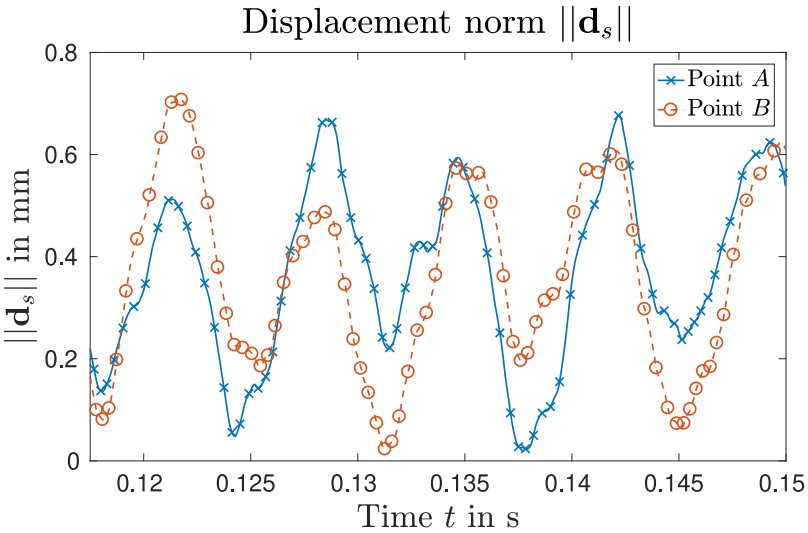

Fig. 21. Human phonation example: displacement norm $\|\boldsymbol{d}_s\|$ in the apex points A ($\times$) and B ($\circ$) showing the multi-modal, non-symmetric motion of the two VFs.

The resulting velocity field is characterised by high velocity gradients, vortices of variable size and pressure fluctuations. Especially during the closing phase, the narrow channel and high onset pressure trigger a strong jet as shown in Fig. 22. Note that choosing a lower stiffness or higher flow rate can result in the VFs getting too close, which inevitably leads to the breakdown of the ALE algorithm.

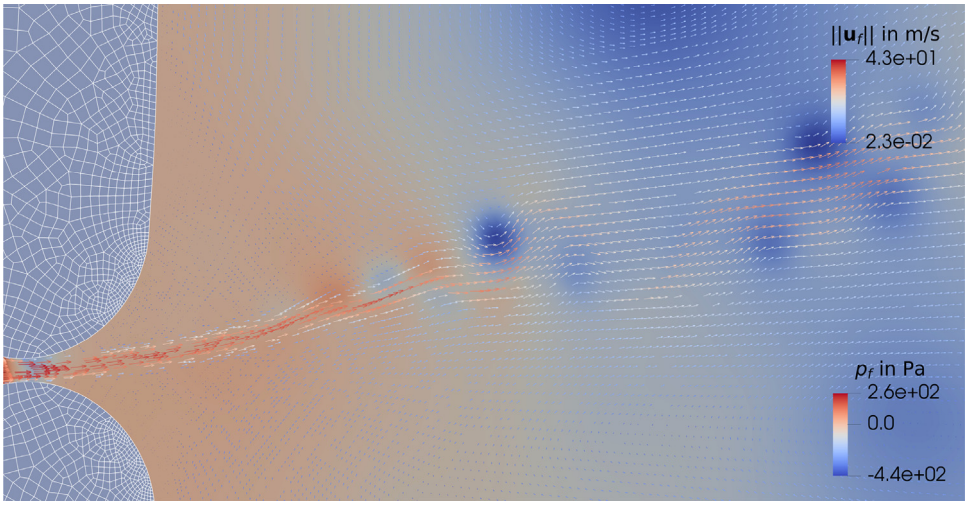

Fig. 22. Human phonation example: selected velocity vectors $\boldsymbol{u}_f$ over pressure p_f and deformed solid mesh during the closing phase of the VFs causing high velocities and pressure fluctuations.

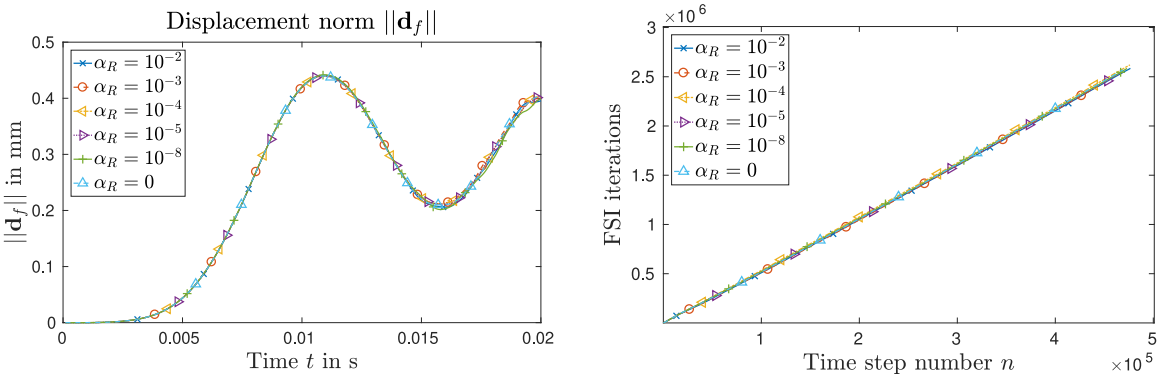

Fig. 23. Human phonation example: varying the Robin parameter $\eta_s^R = \alpha_R \frac{\rho_f}{\Delta t^n}$ has little influence on $\boldsymbol{d}_f$ in the glottal channel centre (left) and the accumulated FSI iterations (right).

Table 8
Human phonation example: Mean FSI iteration counts depending on Robin parameter scaling α_R.

α_R	10^{-2}	10^{-3}	10^{-4}	10^{-5}	10^{-8}	0
Mean FSI iter./step	5.42	5.42	5.50	5.43	5.46	5.48

Turning our attention to the FSI coupling schemes' performance, we observe an almost constant number of FSI iterations per time step, as indicated by the straight line in Fig. 23. Roughly $4.7 \cdot 10^5$ time steps are executed, which gives an average time step size of $3.2 \cdot 10^{-7}$ s to fulfil $\mathrm{CFL}_{\max} < 0.2$ and with a mean of 5.48 FSI iterations per time step, this yields $2.56 \cdot 10^6$ iterations in the semi-implicit coupling loop. Varying the Robin parameter, we see no significant effect on the FSI iteration count, as indicated by Table 8. Similar to the previous examples in the haemodynamic context, though, a Robin parameter too high might impair stability via the increased weight on the explicit contributions to the interface Robin terms. Hence, using a Robin condition is not recommended in this context, even though only mild differences in the solution are seen, as shown in Fig. 23 for the interval $t = 0$ to $t = 0.02$ s. The large number of time steps leads to bigger differences as time progresses, owing to the loose tolerance settings and nonlinear influence of past time step data.

Summing up, this last numerical experiment demonstrates the versatility of the semi-implicit coupling scheme by applying it in the context of aeroelasticity. The split-step scheme with GLS and backflow stabilisations shows great robustness with respect to the changes in the physical parameters. The semi-implicit coupling scheme and the IQN-ILS acceleration perform well reusing the parameters from the haemodynamic setting. However, performance gains as impressive as presented in the previous numerical tests cannot be expected, since the added-mass effect becomes less influential as $\rho_s \gg \rho_f$. A semi-implicit coupling scheme is used nonetheless, since instabilities accumulate over time and, consequently, a fully-explicit scheme turned out not to be sufficiently robust.

6. Concluding remarks

Within this work, we have extended our partitioned PPE-based ALE FSI scheme [52] by several numerical techniques and modelling aspects of practical relevance in biomedical applications. An added-mass-stable, semi-implicit algorithm is employed, iteratively coupling merely the fluid pressure obtained from a (consistent) Poisson equation and the structural displacement. The mesh motion equation, fluid momentum balance, Leray projection and pressure boundary data projection are only solved once per time step. This alone leads to significant speed-up, but is further combined with Robin interface conditions in the solid subproblem and IQN-ILS acceleration. This greatly increases robustness and performs substantially better than comparable acceleration methods such as Aitken's relaxation and each of the involved techniques on their own.

Our numerical experiments suggest that the influence of the Robin parameter on the solution vanishes with decreasing time step size, such that one might really profit from accelerated convergence and increased robustness, while the solution is close to the reference Dirichlet–Neumann coupling scheme. This allows tackling problems of practical relevance with acceptable Robin parameters, which is particularly advantageous when comparing the proposed scheme to fully explicit FSI schemes based on Nitsche-type mortaring or Robin–Robin coupling.

A smooth transition from Dirichlet–Robin to Dirichlet–Neumann schemes without ill-conditioning of the linear systems is possible, simply choosing $\eta_s^R = 0$. Thus, selecting a suitable Robin parameter is less critical and a low number of coupling iterations results also for the IQN-ILS-accelerated semi-implicit Dirichlet–Neumann scheme. This versatility is seen as an advantage over explicit (often only first-order accurate) FSI schemes, which rely on a suitable Robin parameter for temporal stability.

Moreover, adaptive timestepping based on the CFL number is employed, cutting down the number of needed time steps drastically, while only mildly affecting the coupling schemes' performance. Other indispensable numerical techniques in the context of cardiovascular simulations are GLS and backflow stabilisation, which need to be considered in a suitable fashion in the semi-implicit FSI solver to preserve consistency.

Another important contribution here deals with advanced modelling aspects and parameters highly relevant for patient-specific simulations. Windkessel models to account for the downstream vasculature in truncated haemodynamic systems are incorporated in a fully consistent way, modifying the PPE and fluid momentum steps. Further, we present an algorithm to suitably generate local material orientations, rendering anisotropic material models really applicable in scenarios such as aortic dissection, where a thin tissue layer separates the cross section into two distinct lumina. Lastly, we document details on a prestressing algorithm to account for loaded reference geometries and how it can be included in the overall FSI algorithm. Concerning material models, generalised Newtonian fluids and a quasi-incompressible, hyperelastic tissue model including fibre-reinforcement and viscoelastic support is considered, both of which are easily exchanged owing to the partitioned design.

To sum up, we present an efficient (in terms of total coupling steps and their cost) and highly flexible (with respect to material parameters and target applications) FSI algorithm, which includes all necessary model aspects to tackle realistic, patient-specific problems. We demonstrate the versatility and success of the proposed schemes in aortic blood flow and human phonation.

Declaration of competing interest

The authors declare that they have no known competing financial interests or personal relationships that could have appeared to influence the work reported in this paper.

Data availability

Data will be made available on request.

Acknowledgement

The authors gratefully acknowledge Graz University of Technology, Austria for the financial support of the Lead-project: Mechanics, modelling and Simulation of Aortic Dissection.

References

[1] P. Crosetto, P. Reymond, S. Deparis, D. Kontaxakis, N. Stergiopulos, A. Quarteroni, Fluid–structure interaction simulation of aortic blood flow, Comput. Fluids 43 (1) (2011) 46–57.
[2] K. Bäumler, V. Vedula, A. Sailer, J. Seo, P. Chiu, G. Mistelbauer, F. Chan, M. Fischbein, A. Marsden, D. Fleischmann, Fluid–structure interaction simulations of patient-specific aortic dissection, Biomech. Model Mechanobiol. 19 (5) (2020) 1607–1628.
[3] R. Schussnig, M. Rolf-Pissarczyk, G. Holzapfel, T.-P. Fries, Fluid-structure interaction simulations of aortic dissection, PAMM 20 (1) (2021).
[4] S. Thomson, L. Mongeau, S. Frankel, Aerodynamic transfer of energy to the vocal folds, J. Acoust. Soc. Am. 118 (3) (2005) 1689–1700.
[5] M. de Oliveira Rosa, J. Pereira, M. Grellet, A. Alwan, A contribution to simulating a three-dimensional larynx model using the finite element method, J. Acoust. Soc. 114 (5) (2003) 2893–2905.
[6] H. Luo, R. Mittal, S. Bielamowicz, Analysis of flow-structure interaction in the larynx during phonation using an immersed-boundary method, J. Acoust. Soc. 126 (2) (2009) 816–824.
[7] C. Tao, J. Jiang, Y. Zhang, Simulation of vocal fold impact pressures with a self-oscillating finite-element model, J. Acoust. Soc. 119 (6) (2006) 3987–3994.
[8] W. Wall, T. Rabczuk, Fluid–structure interaction in lower airways of CT-based lung geometries, Internat. J. Numer. Methods Fluids 57 (5) (2008) 653–675.
[9] U. Küttler, M. Gee, C. Förster, A. Comerford, W. Wall, Coupling strategies for biomedical fluid-structure interaction problems, Int. J. Numer. Methods Biomed. Eng. 26 (2010) 305–321.
[10] M. Heil, An efficient solver for the fully coupled solution of large-displacement fluid–structure interaction problems, Comput. Methods Appl. Mech. Engrg. 193 (1–2) (2004) 1–23.
[11] A. Quaini, A. Quarteroni, A semi-implicit approach for fluid-structure interaction based on an algebraic fractional step method, Math. Models Methods Appl. Sci. 17 (06) (2007) 957–983.
[12] J. Donea, S. Giuliani, J. Halleux, An arbitrary Lagrangian-Eulerian finite element method for transient dynamic fluid-structure interactions, Comput. Methods Appl. Mech. Engrg. 33 (1–3) (1982) 689–723.
[13] J. Brandsen, A. Viré, S. Turteltaub, G. Van Bussel, A comparative analysis of Lagrange multiplier and penalty approaches for modelling fluid-structure interaction, Eng. Comput. 38 (4) (2021) 1677–1705.
[14] C. Hesch, A. Gil, A. Arranz Carreño, J. Bonet, P. Betsch, A mortar approach for fluid–structure interaction problems: Immersed strategies for deformable and rigid bodies, Comput. Methods Appl. Mech. Engrg. 278 (2014) 853–882.
[15] F. Baaijens, A fictitious domain/mortar element method for fluid-structure interaction, Internat. J. Numer. Methods Fluids 35 (7) (2001) 743–761.
[16] D. Boffi, L. Gastaldi, A fictitious domain approach with Lagrange multiplier for fluid-structure interactions, Numer. Math. 135 (3) (2017) 711–732.
[17] M. Mayr, M. Noll, M. Gee, A hybrid interface preconditioner for monolithic fluid–structure interaction solvers, Adv. Model Simul. Eng. Sci. 7 (1) (2020) 15.
[18] P. Crosetto, S. Deparis, G. Fourestey, A. Quarteroni, Parallel algorithms for fluid-structure interaction problems in haemodynamics, SIAM J. Sci. Comput. 33 (4) (2011) 1598–1622.
[19] A. Massing, M. Larson, A. Logg, M. Rognes, A Nitsche-based cut finite element method for a fluid-structure interaction problem, Comm. App. Math. Comp. Sci. 10 (2) (2015) 97–120.
[20] E. Burman, M. Fernández, S. Frei, A Nitsche-based formulation for fluid-structure interactions with contact, Esaim Math. Model Numer. Anal. 54 (2) (2020) 531–564.
[21] T. Klöppel, A. Popp, U. Küttler, W. Wall, Fluid–structure interaction for non-conforming interfaces based on a dual mortar formulation, Comput. Methods Appl. Mech. Engrg. 200 (45–46) (2011) 3111–3126.
[22] Y. Kim, C. Peskin, A penalty immersed boundary method for a rigid body in fluid, Phys. Fluids 28 (3) (2016) 033603.
[23] A. Viré, J. Xiang, C. Pain, An immersed-shell method for modelling fluid–structure interactions, Philos. Trans. R. Soc. A 373 (2035) (2015) 20140085.
[24] J. Hron, S. Turek, A monolithic FEM/Multigrid solver for an ALE formulation of fluid-structure interaction with applications in biomechanics, in: Fluid-Structure Interaction, Springer Berlin Heidelberg, Berlin, Heidelberg, 2006, pp. 146–170.
[25] T. Wick, Fully Eulerian fluid–structure interaction for time-dependent problems, Comput. Methods Appl. Mech. Engrg. 255 (2013) 14–26.
[26] R. Schussnig, T.-P. Fries, A concept for aortic dissection with fluid-structure-crack interaction, PAMM 19 (1) (2019).
[27] D. Jodlbauer, U. Langer, T. Wick, Parallel block-preconditioned monolithic solvers for fluid-structure interaction problems, Int. J. Numer. Methods Eng. 117 (6) (2019) 623–643.
[28] U. Küttler, W. Wall, Fixed-point fluid–structure interaction solvers with dynamic relaxation, Comput. Mech. 43 (1) (2008) 61–72.
[29] S. Badia, F. Nobile, C. Vergara, Fluid–structure partitioned procedures based on Robin transmission conditions, J. Comput. Phys. 227 (14) (2008) 7027–7051.
[30] M. Gee, U. Küttler, W. Wall, Truly monolithic algebraic multigrid for fluid-structure interaction, Int. J. Numer. Methods Eng. 85 (8) (2011) 987–1016.

[31] P. Causin, J. Gerbeau, F. Nobile, Added-mass effect in the design of partitioned algorithms for fluid–structure problems, Comput. Methods Appl. Mech. Engrg. 194 (42–44) (2005) 4506–4527.
[32] C. Förster, W. Wall, E. Ramm, Artificial added mass instabilities in sequential staggered coupling of nonlinear structures and incompressible viscous flows, Comput. Methods Appl. Mech. Engrg. 196 (7) (2007) 1278–1293.
[33] J. Degroote, K.-J. Bathe, J. Vierendeels, Performance of a new partitioned procedure versus a monolithic procedure in fluid–structure interaction, Comput. Struct. 87 (11–12) (2009) 793–801.
[34] T. Spenke, N. Hosters, M. Behr, A multi-vector interface quasi-Newton method with linear complexity for partitioned fluid–structure interaction, Comput. Methods Appl. Mech. Engrg. 361 (2020) 112810.
[35] J.-F. Gerbeau, M. Vidrascu, A quasi-Newton algorithm based on a reduced model for fluid-structure interaction problems in blood flows, Esaim Math. Model Numer. Anal. 37 (4) (2003) 631–647.
[36] C. Michler, E. van Brummelen, R. de Borst, An interface Newton-Krylov solver for fluid-structure interaction, Internat. J. Numer. Methods Fluids 47 (10–11) (2005) 1189–1195.
[37] J. Degroote, A. Swillens, P. Bruggeman, R. Haelterman, P. Segers, J. Vierendeels, Simulation of fluid-structure interaction with the interface artificial compressibility method, Int. J. Numer. Method Biomed. Eng. 26 (3–4) (2010) 276–289.
[38] A. Bogaers, S. Kok, B. Reddy, T. Franz, Extending the robustness and efficiency of artificial compressibility for partitioned fluid–structure interactions, Comput. Methods Appl. Mech. Engrg. 283 (2015) 1278–1295.
[39] M. Fernández, J.-F. Gerbeau, C. Grandmont, A projection semi-implicit scheme for the coupling of an elastic structure with an incompressible fluid, Int. J. Numer. Methods Eng. 69 (4) (2007) 794–821.
[40] S. Badia, A. Quaini, A. Quarteroni, Splitting methods based on algebraic factorization for fluid-structure interaction, SIAM J. Sci. Comput. 30 (4) (2008) 1778–1805.
[41] M. Astorino, F. Chouly, M. Fernández, Robin based semi-implicit coupling in fluid-structure interaction: Stability analysis and numerics, SIAM J. Sci. Comput. 31 (6) (2010) 4041–4065.
[42] A. Naseri, O. Lehmkuhl, I. Gonzalez, E. Bartrons, C. Pérez-Segarra, A. Oliva, A semi-implicit coupling technique for fluid–structure interaction problems with strong added-mass effect, J. Fluids Struct. 80 (2018) 94–112.
[43] F. Nobile, C. Vergara, An effective fluid-structure interaction formulation for vascular dynamics by generalized Robin conditions, SIAM J. Sci. Comput. 30 (2) (2008) 731–763.
[44] G. Guidoboni, R. Glowinski, N. Cavallini, S. Canic, Stable loosely-coupled-type algorithm for fluid–structure interaction in blood flow, J. Comput. Phys. 228 (18) (2009) 6916–6937.
[45] M. Lukáčová-Medvid'ová, G. Rusnáková, A. Hundertmark-Zaušková, Kinematic splitting algorithm for fluid–structure interaction in hemodynamics, Comput. Methods Appl. Mech. Engrg. 265 (2013) 83–106.
[46] M. Fernández, M. Landajuela, M. Vidrascu, Fully decoupled time-marching schemes for incompressible fluid/thin-walled structure interaction, J. Comput. Phys. 297 (2015) 156–181.
[47] E. Burman, M. Fernández, Stabilization of explicit coupling in fluid–structure interaction involving fluid incompressibility, Comput. Methods Appl. Mech. Engrg. 198 (5–8) (2009) 766–784.
[48] J. Banks, W. Henshaw, D. Schwendeman, An analysis of a new stable partitioned algorithm for FSI problems. part I: Incompressible flow and elastic solids, J. Comput. Phys. 269 (2014) 108–137.
[49] D. Serino, J. Banks, W. Henshaw, D. Schwendeman, A stable added-mass partitioned (AMP) algorithm for elastic solids and incompressible flow: Model problem analysis, SIAM J. Sci. Comput. 41 (4) (2019) A2464–A2484.
[50] G. Gigante, C. Vergara, On the choice of interface parameters in Robin–Robin loosely coupled schemes for fluid–structure interaction, Fluids 6 (6) (2021) 213.
[51] C. Bertoglio, A. Caiazzo, M. Fernández, Fractional-step schemes for the coupling of distributed and lumped models in hemodynamics, SIAM J. Sci. Comput. 35 (3) (2013) B551–B575.
[52] R. Schussnig, D. Pacheco, T.-P. Fries, Efficient split-step schemes for fluid–structure interaction involving incompressible generalised Newtonian flows, Comput. Struct. 260 (2022) 106718.
[53] C.-H. Bruneau, P. Fabrie, Effective downstream boundary conditions for incompressible Navier–Stokes equations, Internat. J. Numer. Methods Fluids 19 (8) (1994) 693–705.
[54] T. Hughes, L. Franca, A new finite element formulation for computational fluid dynamics: VII. The Stokes problem with various well-posed boundary conditions: Symmetric formulations that converge for all velocity/pressure spaces, Comput. Methods Appl. Mech. Engrg. 65 (1) (1987) 85–96.
[55] K. Takizawa, J. Christopher, T. Tezduyar, S. Sathe, Space–time finite element computation of arterial fluid-structure interactions with patient-specific data, Int. J. Numer. Methods Biomed. Eng. 26 (1) (2010) 101–116.
[56] M. Hsu, Y. Bazilevs, Blood vessel tissue prestress modeling for vascular fluid–structure interaction simulation, Finite Elem. Anal. Des. 47 (6) (2011) 593–599.
[57] T. Gasser, R. Ogden, G. Holzapfel, Hyperelastic modelling of arterial layers with distributed collagen fibre orientations, J. R. Soc. Interface 3 (6) (2006) 15–35.
[58] G. Galdi, R. Rannacher, A. Robertson, S. Turek, Hemodynamical Flows, in: Oberwolfach Seminars, vol. 37, Birkhäuser, Basel, 2008.
[59] D. Pacheco, R. Schussnig, T.-P. Fries, An efficient split-step framework for non-Newtonian incompressible flow problems with consistent pressure boundary conditions, Comput. Methods Appl. Mech. Engrg. 382 (2021) 113888.
[60] J. Liu, Open and traction boundary conditions for the incompressible Navier–Stokes equations, J. Comput. Phys. 228 (19) (2009) 7250–7267.
[61] N. Newmark, A method of computation for structural dynamics, J. Eng. Mech. 85 (EM3) (1959) 67–94.
[62] H. Hilber, T. Hughes, R. Taylor, Improved numerical dissipation for time integration algorithms in structural dynamics, Earthq. Eng. Struct. Dyn. 5 (3) (1977) 283–292.

[63] W. Wood, M. Bossak, O. Zienkiewicz, An alpha modification of Newmark's method, Int. J. Numer. Methods Eng. 15 (10) (1980) 1562–1566.
[64] J. Chung, G. Hulbert, A time integration algorithm for structural dynamics with improved numerical dissipation: The generalized-α method, J. Appl. Mech. Trans. ASME 60 (2) (1993) 371–375.
[65] E. Hairer, S. Nørsett, G. Wanner, Solving Ordinary Differential Equations 1 - Nonstiff Problems, Springer, Berlin, 1993.
[66] B. Hübner, D. Dinkler, A simultaneous solution procedure for strong interactions of generalized Newtonian fluids and viscoelastic solids at large strains, Int. J. Numer. Methods Eng. 64 (7) (2005) 920–939.
[67] D. Pacheco, R. Schussnig, O. Steinbach, T.-P. Fries, A global residual-based stabilization for equal-order finite element approximations of incompressible flows, Int. J. Numer. Methods Eng. 122 (8) (2021) 2075–2094.
[68] R. Schussnig, D. Pacheco, T.-P. Fries, Robust stabilised finite element solvers for generalised Newtonian fluid flows, J. Comput. Phys. 442 (2021) 110436.
[69] J. Degroote, Partitioned simulation of fluid-structure interaction, Arch. Comput. Methods Eng. 20 (3) (2013) 185–238.
[70] O. Frank, Die grundform des arteriellen pulses: Mathematische analyse. Erste abhandlung, Z. Biol. (37) (1899) 483–586.
[71] J. Bayer, R. Blake, G. Plank, N. Trayanova, A novel rule-based algorithm for assigning myocardial fiber orientation to computational heart models, Ann. Biomed. Eng. 40 (10) (2012) 2243–2254.
[72] R. Schussnig, K. Bäumler, T.-P. Fries, Multi-layered tissue models in patient-specific simulations of aortic dissection, PAMM 21 (1) (2021) e202100090.
[73] S. Sherifova, G. Holzapfel, Biomechanics of aortic wall failure with a focus on dissection and aneurysm: A review, Acta Biomater. 99 (2019) 1–17.
[74] R. Erbel, F. Alfonso, C. Boileau, O. Dirsch, B. Eber, A. Haverich, H. Rakowski, J. Struyven, K. Radegran, U. Sechtem, J. Taylor, C. Zollikofer, W.W. Klein, B. Mulder, L.A. Providencia, Diagnosis and management of aortic dissection, Eur. Heart J. 22 (18) (2001) 1642–1681.
[75] P.D. Patel, R.R. Arora, Pathophysiology, diagnosis, and management of aortic dissection, Ther. Adv. Cardiovasc. Dis. 2 (6) (2008) 439–468.
[76] R. Schussnig, T.-P. Fries, Coupled multiphysics modeling of aortic dissection, 2020, Paper presented at the 14th WCCM & ECCOMAS Congress 2020, Virtual Congress, 11–15 January 2021.
[77] M. Gee, C. Förster, W. Wall, A computational strategy for prestressing patient-specific biomechanical problems under finite deformation, Int. J. Numer. Methods Biomed. Eng. 26 (1) (2010) 52–72.
[78] T. Tezduyar, S. Sathe, M. Schwaab, B. Conklin, Arterial fluid mechanics modeling with the stabilized space–time fluid–structure interaction technique, Internat. J. Numer. Methods Fluids 57 (5) (2008) 601–629.
[79] D. Arndt, W. Bangerth, B. Blais, M. Fehling, R. Gassmöller, T. Heister, L. Heltai, U. Köcher, M. Kronbichler, M. Maier, P. Munch, J.-P. Pelteret, S. Proell, K. Simon, B. Turcksin, D. Wells, J. Zhang, The deal.II library, Version 9.3, J. Numer. Math. 29 (3) (2021) 171–186.
[80] M. Heroux, J. Willenbring, A new overview of the Trilinos project, Sci. Program 20 (2) (2012) 83–88.
[81] M. Rolf-Pissarczyk, K. Li, D. Fleischmann, G. Holzapfel, A discrete approach for modeling degraded elastic fibers in aortic dissection, Comput. Methods Appl. Mech. Engrg. 373 (2021) 113511.
[82] H. Weisbecker, D. Pierce, P. Regitnig, G. Holzapfel, Layer-specific damage experiments and modeling of human thoracic and abdominal aortas with non-atherosclerotic intimal thickening, J. Mech. Behav. Biomed. Mater. 12 (2012) 93–106.
[83] S. Kim, Y. Cho, A. Jeon, B. Hogenauer, K. Kensey, A new method for blood viscosity measurement, J. Nonnewton. Fluid Mech. 94 (1) (2000) 47–56.
[84] Y. Jin, A. Pepe, J. Li, C. Gsaxner, F. Zhao, J. Kleesiek, A. Frangi, J. Egger, AI-based aortic vessel tree segmentation for cardiovascular diseases treatment: Status Quo, 2021.
[85] C. Dionysio, D. Wild, A. Pepe, C. Gsaxner, J. Li, L. Alvarez, J. Egger, A cloud-based centerline algorithm for studierfenster, in: T. Deserno, B. Park (Eds.), Medical Imaging 2021: Imaging Informatics for Healthcare, Research, and Applications, Vol. 11601, SPIE, International Society for Optics and Photonics, Online only, 2021, pp. 201–206.
[86] N. Heller, F. Isensee, K. Maier-Hein, X. Hou, C. Xie, F. Li, Y. Nan, G. Mu, Z. Lin, M. Han, G. Yao, Y. Gao, Y. Zhang, Y. Wang, F. Hou, J. Yang, G. Xiong, J. Tian, C. Zhong, J. Ma, J. Rickman, J. Dean, B. Stai, R. Tejpaul, M. Oestreich, P. Blake, H. Kaluzniak, S. Raza, J. Rosenberg, K. Moore, E. Walczak, Z. Rengel, Z. Edgerton, R. Vasdev, M. Peterson, S. McSweeney, S. Peterson, A. Kalapara, N. Sathianathen, N. Papanikolopoulos, C. Weight, The state of the art in kidney and kidney tumor segmentation in contrast-enhanced CT imaging: Results of the KiTS19 challenge, Med. Image Anal. 67 (2021) 101821.
[87] C. Mills, I. Gabe, J. Gault, D. Mason, J. Ross, E. Braunwald, J. Shillingford, Pressure-flow relationships and vascular impedance in man, Cardiovasc. Res. 4 (4) (1970) 405–417.
[88] S. Kniesburges, S. Thomson, A. Barney, M. Triep, P. Sidlof, J. Horacek, C. Brucker, S. Becker, In Vitro experimental investigation of voice production, Curr. Bioinform. 6 (3) (2011) 305–322.
[89] S. Falk, S. Kniesburges, S. Schoder, B. Jakubaß, P. Maurerlehner, M. Echternach, M. Kaltenbacher, M. Döllinger, 3D-FV-FE aeroacoustic Larynx model for investigation of functional based voice disorders, Front. Physiol. 12 (2021).